Array-based iterative measurements of SmKS travel times and their constraints on outermost core structure

Wenbo Wu[1,2], and Jessica C. E. Irving [1]

[1] Department of Geosciences, Princeton University, Princeton, NJ 08541, USA

[2]Seismological Laboratory, Division of Geological and Planetary Sciences, California Institute of Technology, Pasadena, CA 91125, USA

Key Points:

- We develop an array-based iterative method to measure SmKS-SKKS (m=3-5) differential travel times.
- 3D mantle structure effects must be considered in studies of SmKS differential travel times.
- Our measurements support a low Vp at the top of outer core.

Corresponding author: Wenbo Wu, wenbow@princeton.edu

Abstract

Vigorous convection in Earth's outer core led to the suggestion that it is chemically homogeneous. However, there is increasing seismic evidence for structural complexities close to the outer core's upper and lower boundaries. Both body waves and normal mode data have been used to estimate a P-wave velocity, Vp, at the top of the outer core (the E′ layer), which is lower than that in the Preliminary Reference Earth Model. However, these low Vp models do not agree on the form of this velocity anomaly. One reason for this is the difficulty in retrieving and measuring SmKS arrival times. To address this issue, we propose a novel approach using data from seismic arrays to iteratively measure SmKS-SKKS differential travel times. This approach extracts individual SmKS signal from mixed waveforms of the SmKS series, allowing us to reliably measure differential travel times. We successfully use this method to measure SmKS time delays from earthquakes in the Fiji-Tonga and Vanuatu subduction zones. SmKS time delays are measured by waveform cross-correlation (CC) between SmKS and SKKS and the CC coefficient allows us to access measurement quality. We also apply this iterative scheme to synthetic SmKS seismograms to investigate the 3D mantle structure's effects. The mantle structure corrections are not negligible for our data and neglecting them could bias the Vp estimation of uppermost outer core. After mantle structure corrections, we can still see substantial time delays of S3KS, S4KS and S5KS, supporting a low Vp at the top of Earth's outer core.

1 Introduction

The liquid outer core in the Earth plays a critical role in the geodynamo and in thermochemical interactions between the mantle and core. Seismic studies can provide important constraints on the physical properties of the core and therefore improve our understanding of the composition and state of the core (Hirose et al., 2013). Due to vigorous convection, the bulk of the outer core is believed to be well mixed and therefore chemically homogeneous (Stevenson, 1987). However, there is increasing seismic evidence for structural complexities close to its top and bottom boundaries. A stratified layer with a lower Vp gradient than the Preliminary Reference Earth Model (PREM; Dziewonski & Anderson, 1981), labeled the F-layer, has been documented using body seismic wave observations (Souriau & Poupinet, 1991b; Song & Helmberger, 1995; Zou et al., 2008; Ohtaki & Kaneshima, 2015). Another stratified layer, the E′ layer, is hypothesized to

exist at the top of outer core and its properties may be constrained by geomagnetic secular variations (Gubbins, 2007; Buffett, 2014), but the seismic evidence, especially SmKS differential arrival times, for this layer is contradictory and controversial (e.g. Eaton & Kendall, 2006; Alexandrakis & Eaton, 2010; Helffrich & Kaneshima, 2010; Kaneshima & Helffrich, 2013).

SmKS waves (m=1, 2, 3, ...) travel as S-waves in the mantle, are converted to compressional waves entering the outer core, reflected m-1 times on the underside of the core-mantle boundary (CMB), and reconvert to S-waves to travel through the mantle (Fig. 1a). SmKS waves are sensitive to the structure of outer core and their arrival times have been used to investigate Vp (compressional wave velocity) in the shallow outer core (Choy, 1977). SKS absolute arrival times have a large scatter, especially due to 3D mantle structure (e.g. Garnero et al., 2016), which results in large uncertainties in their constraints on outer core structure. SKKS and SKS have similar raypaths near the source, so their differential arrival times can partially remove the source effects and constrain the Vp of shallow outer core better. Hales & Roberts (1971) compiled SKKS-SKS differential arrival times and found a low Vp in the outermost core. However, the reliability of this study is reduced by the uncorrected phase shifting between SKS and SKKS (Choy & Richards, 1975; Choy, 1977).

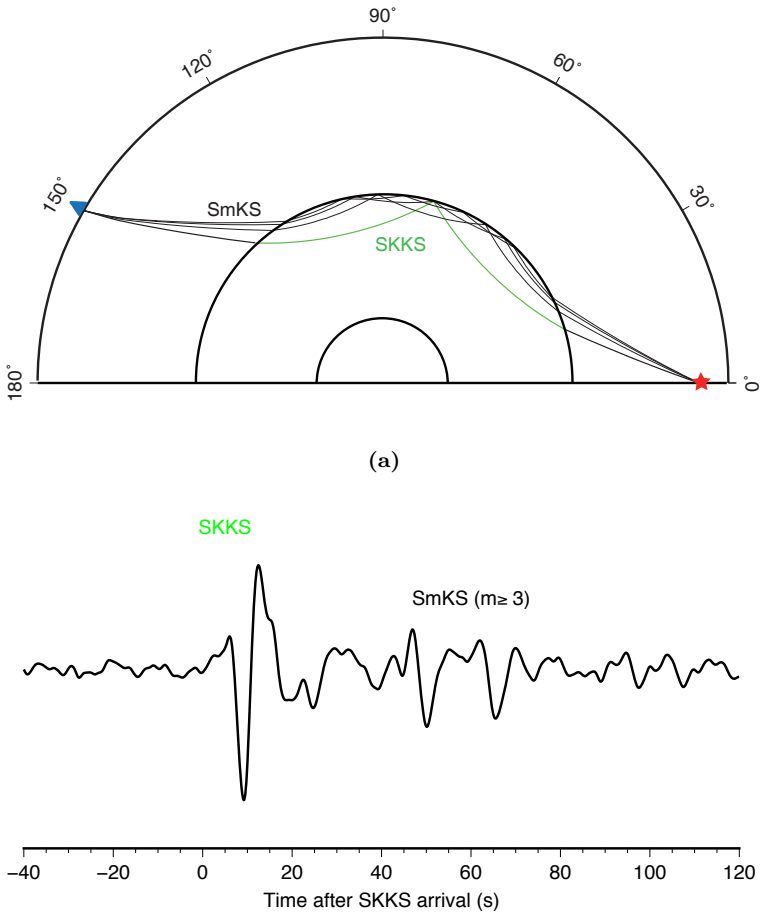

Figure 1: Ray paths of SmKS waves and one example of SmKS waveforms. (a) Ray paths of SmKS. The red star is an earthquake and the blue triangle represents a seismic station. The green line shows the ray path of SKKS traveling in the outer core. The black lines are ray paths of SmKS (m=3, 4 and 5) and sections of SKKS ray path traveling in the mantle and crust. (b) A band-pass filtered (bp 0.05-0.7 Hz) seismogram of SmKS data from station ASSE with an epicentral distance of 150.5° from the event #110729 (Table S1). Time zero is the SKKS arrival predicted by PREM. The predicted arrival time of S3KS is 39 s after SKKS. S4KS arrives at 52 s and S5KS is only 5 s after the S4KS.

Although the ray paths of SKS and SKKS are close to each other near the source, they diverge further in the lower mantle, where lateral heterogeneities could affect their different travel times (Garnero et al., 1988; Souriau & Poupinet, 1991a). Compared to

SKKS and SKS, SmKS and S(m-1)KS with m>2, e.g. S3KS-SKKS, have closer raypaths (Fig. 1a) and therefore their differential arrival times are less affected by 3D mantle structures. With the high quality seismic data accumulated in the last few decades, many more observations of SmKS (m≥2) waves has been reported and their differential travel times have been used to investigate the stratification of the top outer core. However, the conclusions of various studies are not consistent. For example, Alexandrakis & Eaton (2007) exploited the Empirical Transfer Function (ETF) technique to precisely measure SmKS differential travel times and found no evidence for stratification, consistent with some other SmKS studies (e.g. Souriau & Poupinet, 1991a; Alexandrakis & Eaton, 2010). In contrast, other reports support a layer with lower Vp than that of PREM in the outermost core (e.g. Garnero et al., 1993; Tanaka, 2004; Eaton & Kendall, 2006; Tanaka, 2007; Helffrich & Kaneshima, 2010; Kaneshima & Helffrich, 2013; Tang et al., 2015; Kaneshima & Matsuzawa, 2015; Kaneshima, 2018), although the thickness and amplitude of the Vp anomaly varies from one study to another.

There are at least two reasons for the preceding contradictory results. The first one is the difficulty in extracting each individual SmKS phase and precisely measuring the differential arrival times. For high orders $m \geq 3$, SmKS series constitute a whispering-gallery mode and consecutive SmKS phases have very close arrival times (e.g. S4KS and S5KS in Fig. 1a), which makes separating consecutive SmKS waveforms difficult. Another problem is contamination from lateral heterogeneities in mantle structure. Although ray paths of SmKS and S(m-1)KS (m>2) series are closer to each other than that of SKS and SKKS, there are still differences in the mantle, especially the heterogeneous D″ region (Garnero & Helmberger, 1995). These mantle heterogeneities could cause large uncertainty or bias in the differential arrival time measurements made using individual seismograms (Garnero et al., 1993) or small-aperture arrays (Eaton & Kendall, 2006). Stacking of data from large-scale arrays (Helffrich & Kaneshima, 2010; Kaneshima & Helffrich, 2013; Kaneshima & Matsuzawa, 2015; Kaneshima, 2018) or global networks (Alexandrakis & Eaton, 2010) tends to average out perturbations due to mantle heterogeneities and therefore mitigate the possible bias. Alternatively, the bias can be evaluated using ray theory (e.g. Helffrich & Kaneshima, 2010; Kaneshima & Helffrich, 2013; Kaneshima & Matsuzawa, 2015; Kaneshima, 2018) or sophisticated waveform modeling (Tanaka, 2004, 2007), based on either known 3D mantle tomography model or hypothesized structure.

Combining array stacking and accurate 3D mantle corrections would be an optimal solution to suppress 3D mantle effects, which has not been reported before.

To ameliorate these problems, we develop an iterative method to separate individual SmKS phases from the SmKS wavetrain in array data and use normalized cross-correlation (CC) to measure the differential travel times between SmKS (m=3, 4 and 5) and SKKS. We carefully select good quality data to successfully obtain each SmKS phase. The iterative method provides us with accurate waveform-based measurements of differential arrival times and important information to assess the measurement quality. We use two methods, ray theory and the Spectral Element Method (SEM), to investigate the effects of lateral heterogeneities in the mantle, using the 3D tomography model S40RTS (Ritsema et al., 2011), and also assess the effect of choosing a different mantle model (S362ANI Kustowski et al., 2008). The measured differential arrival times, after correction for 3D mantle structure effects, are compared to the predictions of body-wave derived model KHOMC (Kaneshima & Helffrich, 2013) and normal-mode constrained model EPOC (Irving et al., 2018).

2 Data

We collected more than 320,000 seismograms from global stations from 500 earthquakes in the subduction zones of Fiji-Tonga, Vanuatu, New Britain and Solomon with depths$\geq$150 km and Mw$\geq$5.5 (Global Centroid-Moment Tensor catalog, Ekström et al., 2012) in the period 2000-2016 (Supporting Information Fig. S1). We select events with depths $\geq$ 150 km to avoid contamination from depth phases sSmKS (m$\geq$2). The seismograms have a distance range of 120-180°, where waveforms SmKS (m$\geq$2) are readily observed.

We remove instrument responses and rotate the two horizontal components to get the radial displacement, on which SmKS primarily appears. Then a band-pass filter (0.05 - 0.7 Hz) is applied to the data with Signal-Noise Ratio (SNR) computation. From these 500 earthquakes, we find 11 events with a large number of good observations of SKKS (Fig. 2a). Here, good observation means SNR larger than 2, a large number means 100 or more seismograms, and we carefully inspect the data to rule out any possible contamination from small local earthquakes. The SNR is defined as the peak-to-peak amplitude ratio of SKKS to noise. We measure SKKS amplitude in a time window between 20 s

before and 50 s after the SKKS arrival time predicted by PREM (Fig. 3a). The time window of noise is taken between 70 s and 20 s before the SKKS arrival. There are total 3741 radial components from these 11 events and 2535 of them have $SNR_{SKKS} > 2.0$ (Fig. 2b). Limited by the geographic distribution of seismic stations, most of these clear SKKS data are from stations in Europe with a distance range of 140°-160° and their ray paths sample the northeastern Pacific, Asia and Europe.

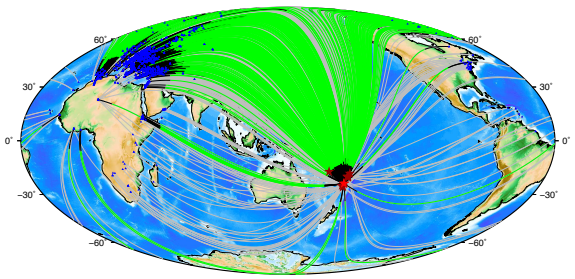

(a)

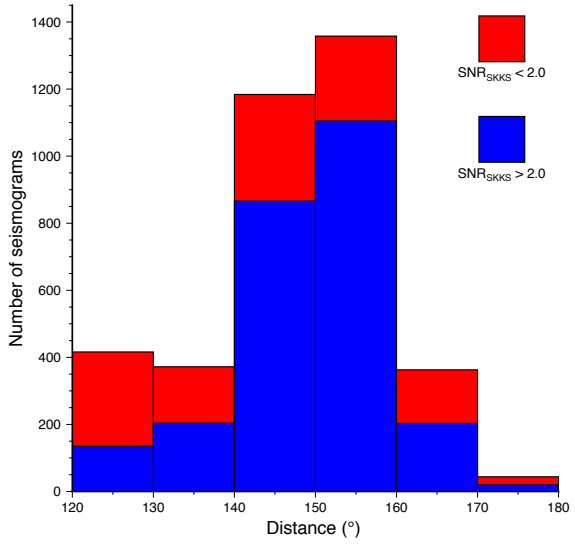

(b)

Figure 2: Map and histogram of clear SmKS data. (a) Map of good SKKS data (SNR≥2.0) from the ten earthquakes. The blue triangles and red stars show the stations and earthquakes, respectively. The lines connecting stations and earthquakes are ray paths of SKKS. The green lines show the ray paths of SKKS traveling in the outer core from the event #110729. (b) Histogram of SKKS data in (a). The blue bar portions correspond to SKKS data with high SNR≥2.0 and the red bar portions show the ones with SNR<2.0.

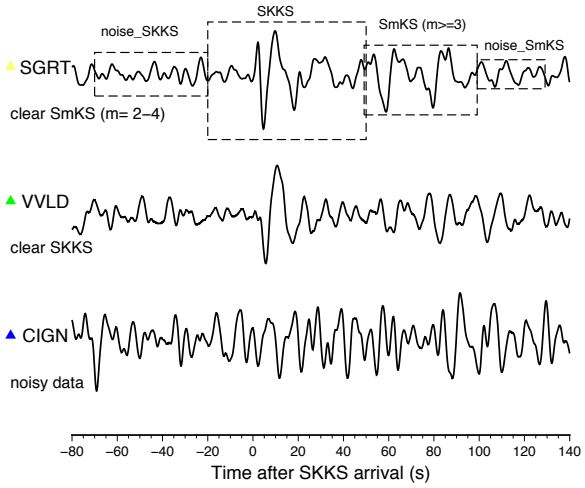

(a)

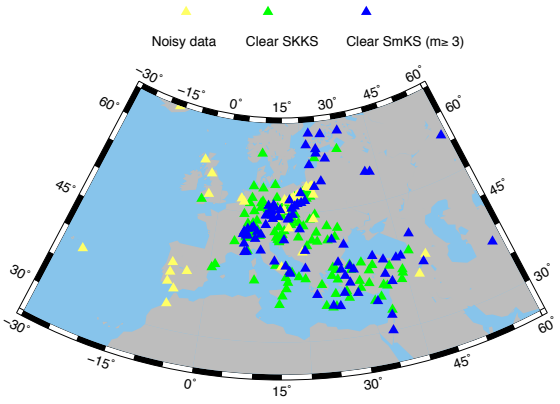

(b)

Figure 3: SmKS data from stations in Europe from event #071016. (a) An example of waveforms with poor SKKS with SNR<2.0 (bottom panel), good SKKS with SNR≥2.0 only (middle panel), and high SNRs for both SmKS (m=3 and higher) and SKKS (top panel). The SNR of SKKS is defined as the peak-to-peak amplitude ratio of SKKS (20 s before to 50 s after the SKKS arrival predicted by PREM) to that of the noise (70 s to 20 s before the SKKS arrival). Similarly, the SNR of SmKS (m≥3) is obtained by measuring SmKS signals (0 s to 50 s after S3KS arrival) and the associated noise (50 s to 85 s after S3KS arrival). The time zero is the SKKS arrival predicted by PREM. (b) Map of stations in Europe from event #071016. Stations with noisy SKKS, good SKKS only and high SNRs for both SmKS (m=3 and higher) and SKKS are shown as yellow, green and blue triangles respectively.

Following previous studies (e.g. Tanaka, 2004; Eaton & Kendall, 2006; Helffrich & Kaneshima, 2010; Alexandrakis & Eaton, 2010; Kaneshima, 2018), we use SKKS as a reference phase to investigate the arrivals of SmKS (m>2), so clear SmKS (m>2) signals are also important for high quality measurements. We compute SNR of SmKS (m>2) and only use the data with clear SmKS ($SNR_{SmKS} \geq 2.0$, see Fig. 3). In contrast to the SNR_{SKKS} computation, we take the noise window starting after the predicted S2KS arrival time for SNR_{SmKS} (by 100 seconds) and some $SmKS$ coda waves are included in this time window. Thus, the data with strong $SmKS$ coda due to significant unwanted source and wave propagation complexities would have low SNR_{SmKS} and therefore be discarded. Then, we use the method described in section 3 to measure these data with clear SmKS (m≥2). Most of our clear data are from Europe and our array-based method needs a number of records to form an array, so here we focus on stations in Europe and north Africa to investigate the SmKS arrivals.

3 Array-based iterative method to measure SmKS-SKKS differential arrival times

3.1 Workflow of the array-based iterative method

SmKS (m≥2) series travel in the mantle and upper outer core, so their arrivals are sensitive to the Vs in the mantle and Vp in the outer core. The ray paths of SKKS and SmKS (m>2) are close to each other in the mantle and further apart in the outer core (Fig. 1a), so taking arrival time differences between SKKS and SmKS (m>2), $t_{SmKS} - t_{SKKS}$, instead of absolute travel time, can significantly reduce the effects of 3D Vs structure in the mantle and improve the constrains on the Vp in outer core. On the other hand, these spatially close ray paths result in small time separations between consecutive SmKS signals, which can make identifying individual SmKS phase and measuring its arrival time difficult. For example, the arrival time difference between S3KS and S4KS at station ASSE from event #110729 is only 13 s (Fig. 1a). The difference between S4KS and S5KS is even smaller and their waveforms are mixed with each other. Many previous efforts have been made to retrieve individual SmKS phase and accurately measure their arrival times (e.g. Eaton & Kendall, 2006; Helffrich & Kaneshima, 2010; Kaneshima & Helffrich, 2013). In particular, array stacking techniques have been used to analyze slownesses and arrival times of SmKS signals (e.g. Eaton & Kendall, 2006; Helffrich & Kaneshima, 2010; Kaneshima & Helffrich, 2013). Here, we take the advantage of the large number of stations with good

data to form one or more arrays or bins and develop an iterative method to retrieve individual SmKS and measure their arrival times. This iterative strategy has been used to extract direct S-waves and CMB reflected ScS waves (Z. Yu et al., 2012).

Arrivals in the SmKS series share many factors, such as source time function, 3D wave propagation effects, site responses etc., due to their similar ray paths in the crust and mantle. Although their ray paths diverge further in the outer core, the outer core is believed to be highly laterally homogeneous. Thus, SKKS and SmKS (m>2) usually have very coherent waveforms (after a $\pi(m-2)/2$ phase shift is applied to SmKS with m=3, 4 and 5). This property helps us significantly simplify the problem and separate individual SmKS waveform. In our iterative method, the reference phase SKKS is assumed to be perfectly coherent with each SmKS (m>2) waveform after the phase-shift is applied and only two unknown parameters, SmKS arrival time anomalies and SmKS/SKKS amplitude ratios, are measured in each iteration. We note that another alternative measuring strategy would be attempting to measure SmKS-S(m-1)KS (i.e. S3KS-SKKS, S4KS-S3KS and S5KS-S4KS), which have even closer raypaths than those of SmKS-SKKS (m=3, 4 and 5). However, this strategy suffers from the problem of weak and noisy reference phases S3KS and S4KS, which would affect the performance of our method. Thus, we choose the clearer SKKS waveforms as the reference phase.

This workflow of our iterative method is composed of data preparation and then iterative measuring (Fig. 4). As described in subsection 2, we set an SNR threshold of 2 for both SKKS and SmKS (m>2) to obtain good quality data. Following (Helffrich & Kaneshima, 2010; Kaneshima & Helffrich, 2013), we divide the clear SmKS data from the same event into several bins and stack traces in each bin to further improve the SNR (an example of one bin is shown in Fig. 5). Before stacking the traces, two steps of CC are carried out on SKKS waveforms to align the data. In the first step of CC, we choose one typical trace (i.e. station with the median distance of the bin) as a template (e.g. black line in Fig. 5b) and compute CC of SKKS between this template and other traces in this bin with shifting times. Then these traces are aligned on the time with the maximum CC values. In the next step, we stack the aligned SKKS with normalized amplitudes to form a new template (e.g. red line in Fig. 5b) and then repeat the CC processing to align the SmKS data again (Fig. 5c). The time window of SKKS used in CC is 5 s before and 30 s after the arrival time of SKKS and the maximum allowed time shift is 5 s. Data with maximum CC coefficients lower than 0.8 are not used in the following

iterative measuring, because their low waveform similarities, due to complex site structure or/and instrumental issues, could decrease the quality of stacking and affect the measurements. In these two steps of alignment, the shifted times are primarily due to 3D structures near the stations, source mislocation and/or clock time errors and these factors are shared by SKKS and SmKS (m>2). Thus, shifting the traces are not expected to significantly affect the measurements of differential arrival times.

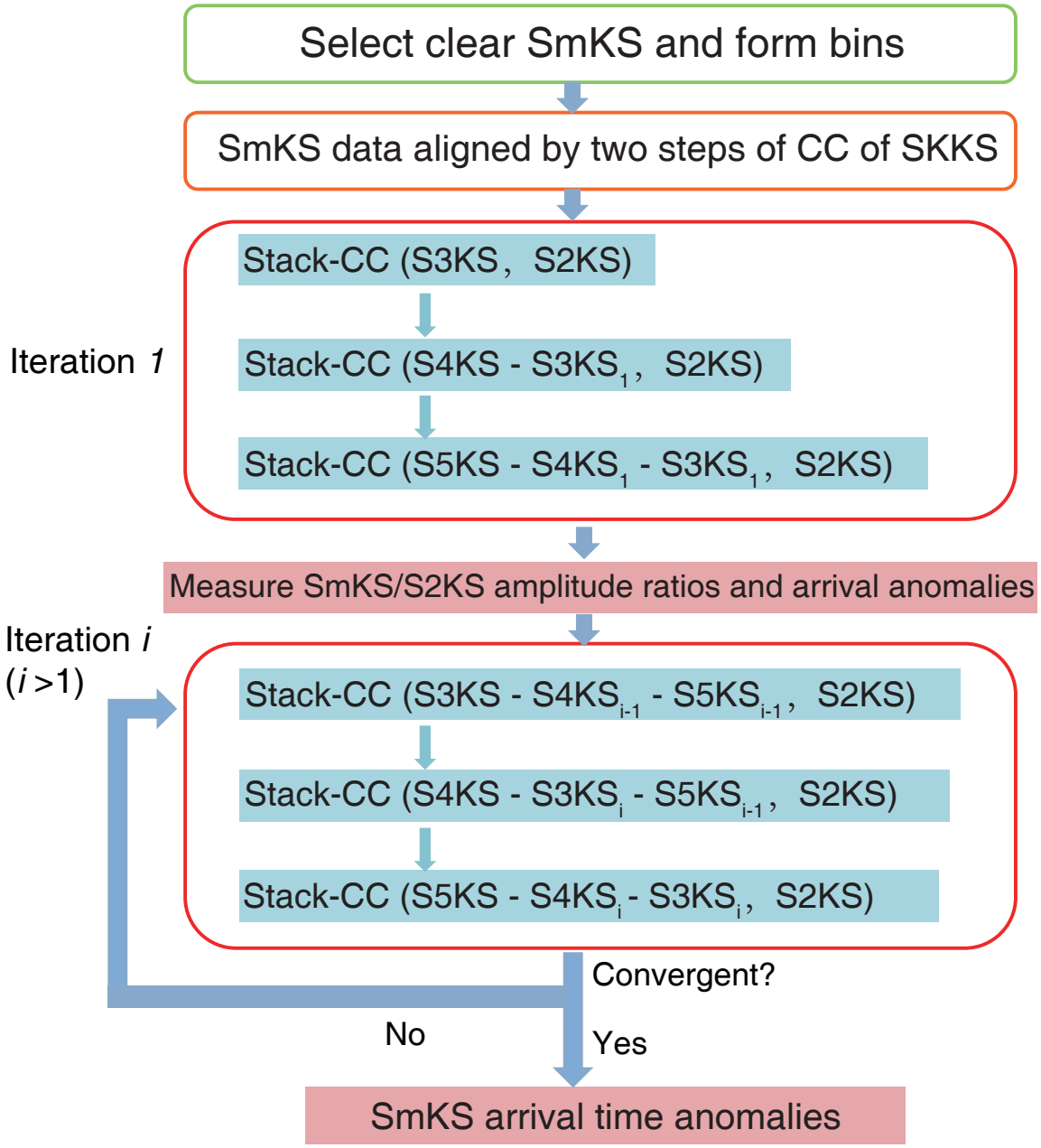

Figure 4: Workflow of the array-based iterative method.

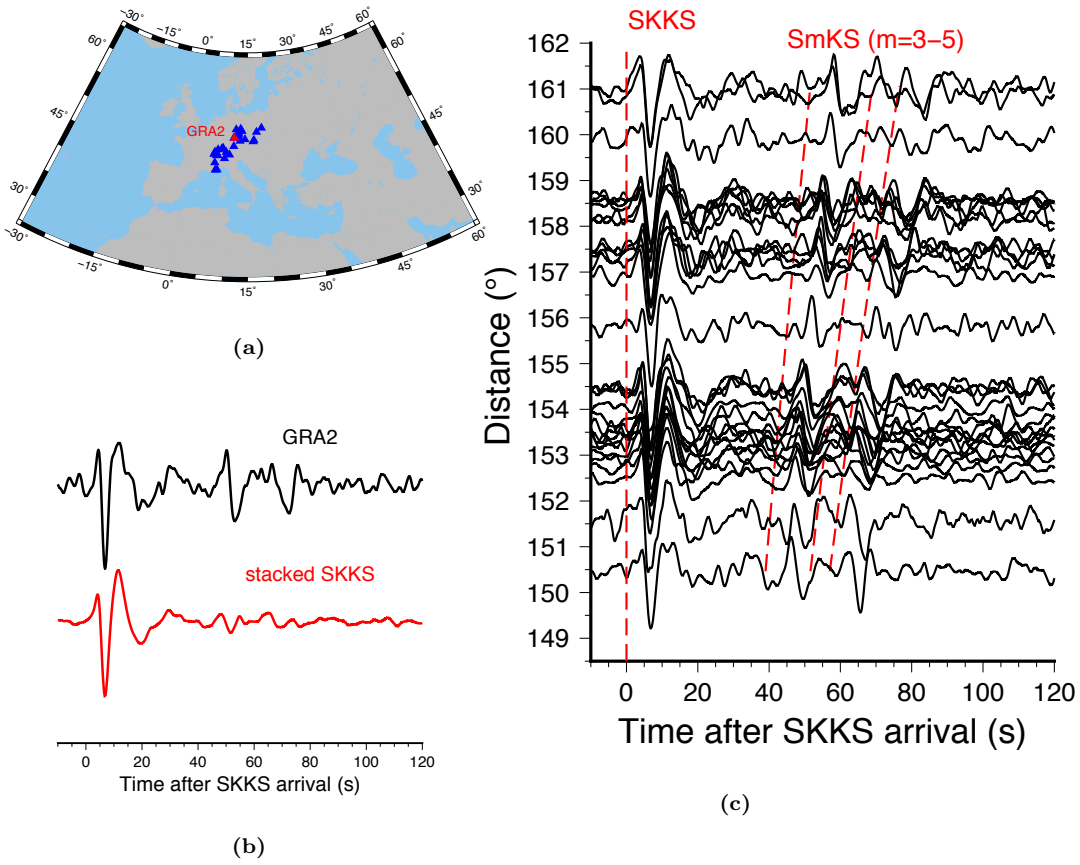

Figure 5: An example of aligning SKKS by two steps of cross-correlation. (a) A map of a bin of stations with clear SmKS from the event #071016. The other stations with clear SmKS are shown in Fig. 2b. (b) The SKKS waveforms from the reference station GRA2 (upper trace, epicentral distance of 154.4°) and stacked SKKS after alignment by CC with GRA2 (lower panel). (c) Distance profile of SmKS data (0.05-0.7 Hz) aligned on SKKS by two steps of CC. The corresponding stations are shown in (a). The time zero is the SKKS arrival. The other red dashed lines are the SmKS (m=3-5) arrivals predicted by PREM.

Next, we use these aligned SmKS data to iteratively retrieve individual SmKS phases, measure differential travel time anomalies and assess quality of each measurement. In the first iteration ("*iteration1*" in Fig. 4), we stack the data in a bin and use three CC processes to measure S3KS, S4KS and S5KS one by one. For S3KS measurement, we stack S3KS using $t_{S3KS}-t_{SKKS}$ predicted by PREM (e.g. see the second red dashed line Fig. 5c), apply the Hilbert transform on them to correct the 90° phase shift and then com-

pute CC between stacked SKKS and S3KS to get S3KS/SKKS amplitude ratio and time delay of S3KS. Then we cut out the SKKS waveform at each station, scale them using the previously measured S3KS/SKKS amplitude ratio and apply the phase shift to get S3KS waveform estimation. This estimated S3KS is subtracted from the data to retrieve a 'clean' S4KS and then a similar stack-CC processing is applied on the retrieved S4KS for measurement. Once S3KS and S4KS have been measured, we can estimate both S3KS and S4KS, remove them in the data and then measure S5KS. After *iteration1*, we obtain initial estimations of SmKS/S2KS (m=3, 4 and 5) amplitude ratios and their time delays. In the next iteration, these information are used to retrieve the target SmKS and more accurately measure them. This iteration is repeated until the measurements are convergent.

This array-based iterative method uses good quality data and has the advantages of enhancing SNR by stacking and retrieving target SmKS signals well by removing other SmKS interfering signals. Note that we use theoretical slowness derived from PREM to stack array data, because Vp anomaly in the uppermost outer core only causes small slowness deviation and slowness measurements could have large uncertainties. A large slowness anomaly would result in less coherent stacking, which would be reflected in the CC coefficient. In the first step of data preparation, we set strict criteria to rule out the data with potential issues that might affect the validity of our method. For example, the requirement of $SNR_{SKKS} \geq 2.0$ allows us discard the data with high noise before SKKS. In addition to that, the other two thresholds of $SNR_{SmKS} \geq 2.0$ and CC$\geq$0.8 rule out more bad quality data (e.g. complex SmKS waveforms and/or strong SmKS coda waves due to 3D heterogeneity or source or station structures). Stacking the data with high CC value further increases SNR and extracting individual SmKS phase from mixed signals allows us reduce uncertainties in measurements. More importantly, this method provides us two critical parameters to assess qualities of measurements. The most important parameter is the CC values between S2KS and target SmKS (S3KS, S4KS and S5KS). A low CC value means a bad quality measurement and we should either discard it, or be careful when using it. Low CC values could be due to a failure of the assumptions we made, weak target signals (e.g. near the nodal plane of radiation pattern of earthquake), insufficient number of traces in a bin etc. In addition to CC values, the amplitude information is also helpful to assess measurement quality. More details are discussed in section 5.

Uncertainty of differential arrival time for each bin is estimated by bootstrapping (Efron & Tibshirani, 1991), which reflects the variance in the bin. For each bin, we randomly select N seismograms, with replacement, from the original N seismograms and measure the differential arrival times. This process is repeated 300 times and we compute the standard deviation of these 300 measurements as an estimation of variance in that bin.

In next section, we demonstrate the validation of our method by testing synthetic seismograms and then apply it to data.

3.2 Synthetic tests

In this subsection, we cut real SKKS waveforms from data, use them to make SmKS (m=2, 3, 4 and 5) synthetics and then validate our iterative method. Fig. 5c shows SmKS data of a bin from event #071016. We cut and taper the SKKS waveforms from 0 s to 40 s as input to generate S3KS, S4KS and S5KS (Fig. 6). S3KS is formed by scaling the input signals with a prescribed S3KS/SKKS amplitude ratio of 0.42, applying a 90° phase shift and a prescribed time shift, which is 1.13 s greater than to the PREM S3KS-SKKS differential arrival time. Similarly, S4KS and S5KS are made with different amplitude ratios and time delays. Then, complete SmKS synthetic seismograms are generated by summing SKKS, S3KS, S4KS and S5KS.

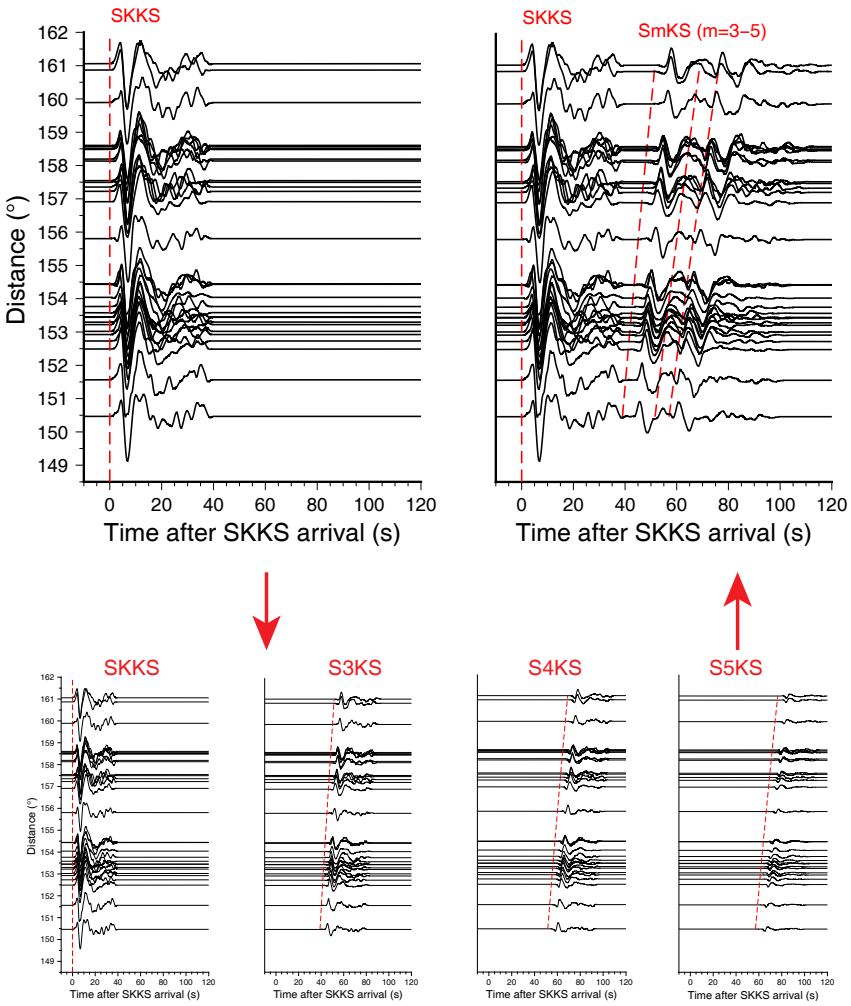

307

308 **Figure 6:** Making SmKS (m=2-5) synthetics using the SKKS data from the event #071016.
309 The upper left figure shows the cut-out and tapered SKKS waveforms (complete data shown in
310 Fig. 5c). Each sub-figure in the lower panel corresponds to the synthetics of individual SmKS
311 phase. We take the tapered SKKS data (upper left figure), scale them using given amplitude
312 ratios and apply the corresponding phase shift and time shift to form each SmKS phase. The
313 S3KS/SKKS amplitude ratio is given as 0.42 and its time delay is 1.13 s. For S4KS, the ampli-
314 tude ratio is 0.31 and the time delay is 2.25 s. For S5KS, the amplitude ratio is 0.14 and the
315 time delay is 2.39 s. These SmKS phases are added together to form the complete synthetics of
316 SmKS series (upper right figure). The dashed red line at the time zero in each figure is the SKKS
317 arrival, the same as Fig. 5c. The other red dashed lines are the SmKS (m=3-5) arrivals predicted
318 by PREM.

Then we apply our iterative method to these synthetic seismograms and check its validity. In the step of searching maximum CC values, we take a time window of 0-30 s after the target SmKS arrival time and the maximum allowed time shift is 5 s. In previous studies, the time delays of SmKS (m=3, 4 or 5) are less than 5 s and most of them are less than 3 s (e.g. Eaton & Kendall, 2006; Helffrich & Kaneshima, 2010; Kaneshima & Helffrich, 2013).

Fig. 7 shows the measurements from the first five iterations. We can see that both amplitude ratios and time delays are successfully retrieved and the CC values for S3KS, S4KS and S5KS are higher than 0.95 after the second iteration. In the first iteration, there are some differences between the measured results and true values. For example, the measured time delay of S4KS is $\sim$ 2.15 s, which is $\sim$ 0.1 s smaller than the input 2.25 s. The CC value for S3KS measurement, $CC_{3,2}$, is 0.88, lower than $CC_{4,2}$=0.92 for S4KS and $CC_{4,2}$=0.92 for S5KS, because the S3KS measurement is affected by the presence of S4KS and S5KS signals. In the second iteration, the CC values are significantly increased and the measurements are close to the true values. The measurements become almost constant in the next three iterations, showing they reach convergence. After the first two iterations, waveforms are successfully retrieved and the time delays are accurately measured (e.g. see the waveform cross-correlations between SKKS and S5KS in Fig. S2). These results demonstrate the validation of our method. Of course, real data may be more complex than the synthetic SmKS here, e.g. different noise signals may be present in data, and therefore measurement quality might be not as good as in these synthetic tests. However, CC values indicate this complexity, demonstrating their importance.

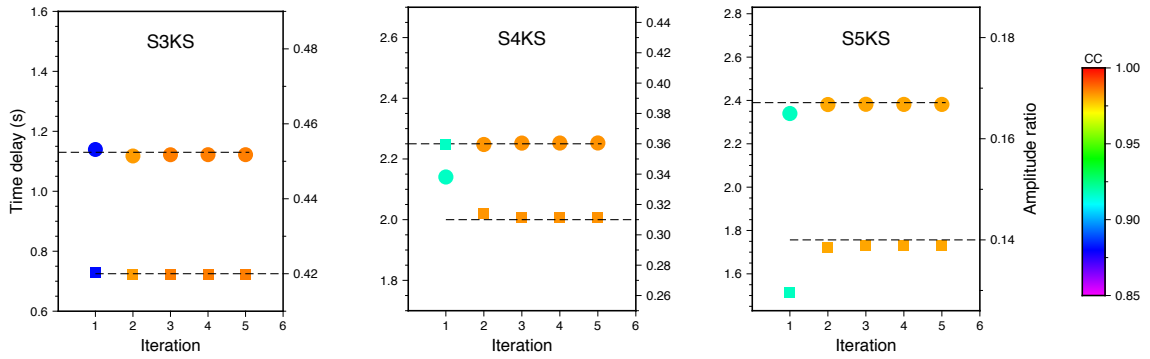

(a) (b) (c)

Figure 7: A synthetic test to validate the array-based iterative method. The colored circles indicate the measured time delay in each iteration. The colored squares are the measured amplitude ratios. The upper black dashed line in each figure is the prescribed time delay and the lower black dashed line corresponds to the given amplitude ratio. Note that the time delays are relative to SmKS-SKKS differential arrival times predicted by PREM. The color represents the CC values between the single SmKS phase and transformed SKKS (e.g. results of S5KS from the first four iterations shown in Fig. S2). Both time delays and amplitude ratios of S3KS, S4KS and S5KS converge to the input values after five iterations and this is also reflected in the high CC coefficients.

3.3 Correcting 3D mantle structure effects

Because the ray paths of SmKS (m=2-5) are close to each other in the mantle, many previous studies assume that the effects of 3D mantle structures are the same for SKKS and SmKS (m>2). Thus, the measured time delays of SmKS (m>2) are only due to the Vp anomalies in the top outer core. However, we know that the ray paths between SKKS and SmKS (m>2) are not exactly the same and the 3D mantle structures must affect the arrival time difference between SKKS and SmKS (m>2). Kaneshima & Matsuzawa (2015) used ray theory to investigate these mantle effects at receiver-side and source-side. At the receiver side, they found that the mantle effects on $dt_{3,2}$ are much less than 0.4 s. However, the presence of a Large Low Shear Velocity Province (LLSVP) beneath the Pacific could cause some time delays of SmKS (m≥2) and affect the measurements.

To investigate 3D mantle effects, we use two different methods, ray theory and SEM, to compute the travel time delays of SmKS and compare their differences. We use SPECFEM3D_globe to compute synthetic seismograms and evaluate the 3D mantle effects present in the tomography models S40RTS (Ritsema et al., 2011) and S362ANI (Kustowski et al., 2008). As a spectral element method, the SPECFEM3D_globe package solves the weak form of the seismic wave propagation equation and has the advantages of high accuracy, fast computation speed, handling discontinuity topography etc. (Komatitsch & Tromp, 1999, 2002; Tromp et al., 2008). The adjoint source technique is part of SPECFEM3D_globe, allowing the efficient computation of global scale sensitivity kernels of seismic signals in a given time window and frequency band (Tromp et al., 2008; Luo et al., 2013). We set the mesh parameters *NEX_XI* and *NEX_ETA* to 896 and the minimum resolved period is about 4.9 s. We use source parameters from GCMT (Global Centroid Moment Tensor, Ekström et al., 2012) and SPECFEM3D_globe to compute the synthetic seismogram and the SmKS travel time sensitivity kernels. We note that GCMT solutions do not contain detailed inversions for source duration, so we reestimate the source duration using teleseismic P-waves from global stations. For comparison, we also compute the 3D mantle structure corrections based on ray theory using the S40RTS model. To simplify the problem, we use PREM to get the ray path and compute the arrival time perturbations along that ray path. In other words, we assume that the ray path is not dramatically distorted by 3D structures.

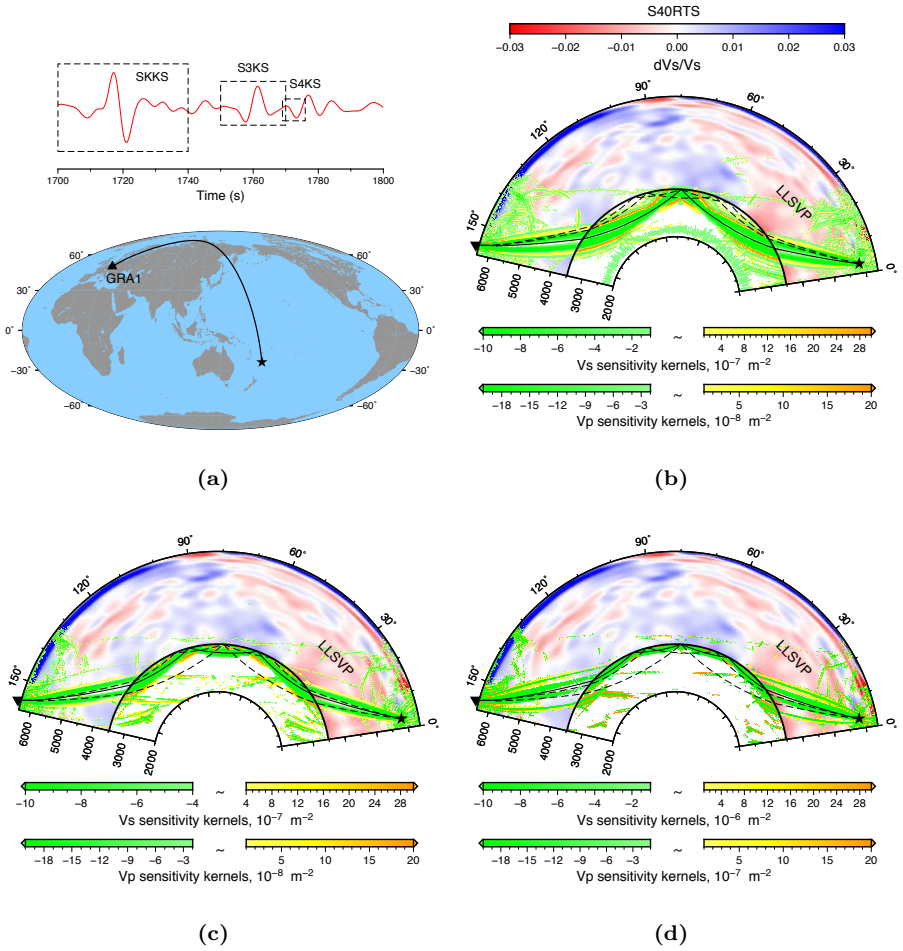

Figure 8: Map and travel time sensitivity kernels of SmKS (m=2-4) at station GRA1 from event #110729. (a) SEM synthetic seismogram (upper panel) and map (lower panel). The red line in the upper figure is the radial component synthetic seismogram of station GRA1 at 0.05-0.2 Hz. The triangle in the map shows the location of station GRA1 and the star is the centroid location of the event #110729. The black line in the map shows the great circle path of SmKS. The arrival times predicted by PREM are 1717.0 s for SKKS, 1758.5 s for S3KS and 1772.1 s for S4KS. The centroid time is 2.5 s, half of our re-estimated duration (Table S1), after the origin time for this event. (b) Travel time sensitivity kernels of SKKS. Sensitivity to Vs is shown in the mantle and to Vp in the core. The red-blue colors illustrate the depth cross-section of dVs/Vs (Vs perturbation) of the 3D model S40RTS. The green-yellow colors show the travel time sensitivity kernels of SKKS and its ray path is plotted with the black line. The dashed black lines are the ray paths of S3KS and S4KS. (c) Travel time sensitivity kernels of S3KS. (d) Travel time sensitivity kernels of S4KS.

Fig. 8 shows a depth cross-section of fractional velocity anomaly, dVs/Vs, from the 3D model S40RTS (Ritsema et al., 2011) along the great circle connecting station GRA1 and event #110729. The ray paths of SmKS (m=2, 3 and 4) sample the LLSVP at the source side, where dVs is lower than -1%. Using this 3D Vs mantle model, we can use ray theory to compute the arrival time anomalies of SmKS (m=2, 3, 4 and 5) along their ray paths. However, ray theory only works at infinite frequency. Indeed, seismic waves at a finite frequency are sensitive to a Fresnel zone, a region centered at its ray path. To demonstrate the Fresnel zones of SmKS, we use the SPECFEM3D_globe package (Komatitsch & Tromp, 1999) to compute sensitivity kernels of SmKS in the mantle and outer core.

Fig. 8a shows the SPECFEM3D_globe synthetic seismogram at GRA1 from the event #110729 and three time windows used to compute the sensitivity kernels of SKKS, S3KS and S4KS. We use the GCMT solution (Ekström et al., 2012) as the input of source parameters, but reestimate its source duration (Fig. S4). The S40RTS model is used to describe mantle heterogeneity and attenuation simulation is disabled to speed up the computation. We use 1536 CPU cores to run the SEM simulation, taking about 14 hours for forward modeling and 27 hours for each adjoint simulation. At frequency 0.05-0.2 Hz, the first Fresnel zone of SKKS (the green band centered at SKKS ray path) has a width of $\sim$ 18 deg ($\sim$ 900 km) on the CMB and its upper boundary approaches the ray paths of S3KS and S4KS (Fig. 8). The sensitivity kernels of S3KS and S4KS have similar dimensions (i.e. the width of the first Fresnel zone), but more complex patterns than SKKS. Compared to SKKS, S3KS and S4KS are more sensitive to the shallower outer core, reflected in the distribution of sensitivity kernels. The wide dimensions and complex patterns of SmKS sensitivity kernels in Fig. 8 indicate that the 3D mantle structure corrections based on ray theory may cause systematic biases and uncertainties. We will discuss the detailed 3D mantle structure correction of each bin and the comparison of ray theory and SEM results in subsection 4.2.

4 Results

4.1 Measuring SmKS-S2KS differential arrival times

We apply the iterative method to data at three frequency bands (0.05-0.2 Hz, 0.05-0.7 Hz and 0.1-0.7 Hz) and investigate the time delays of S3KS, S4KS and S5KS. For

each frequency band, we compute the SNRs (SNR_{SKKS} and SNR_{SmKS}), take clear SmKS data of each event to form bins (one example of event #141101 shown in Fig. S3) and apply the iterative method to each bin.

We only use data at epicentral distances greater than 140°. At shorter distances, S3KS arrival times are close to SKKS (i.e. arrival time difference smaller than 27 s) and therefore might affect quality of cut SKKS waveforms. Based on the number of clear SmKS traces and the station distribution, we divide the data from each event into several geographical bins. For example, the event #141101 provides more than 100 clear SmKS traces (0.05-0.2 Hz) and we divide them into four bins (see Table S1 and Fig. S3). For some bins (e.g. bin 2 from event #010526 in Table S1), the number of clear SmKS traces is too few (i.e. <10) to provide reliable measurements, so we do not use the results of these bins.

At frequencies 0.05-0.2 Hz, we eventually have twenty five effective bins from the eleven events (Table S1). We use the same parameters (i.e. a time window of 40 s to cut SKKS and 30 s for CC computation) as in synthetic testing and apply the iterative method to each bin. In the synthetic testing, the measured results are almost constant after the second iteration. Thus, here we conduct six iterations and take the results from the fifth iteration (detailed measurements listed in Table S1). For each bin, we check the results and make sure that there is no substantial difference between the fourth and fifth and six iterations. In the twenty five bins, the measured S3KS time delay, $dt_{3,2}$, ranges from -0.03 s to 2.83 s and the S3KS/SKKS amplitude ratios, $A_{3,2}$, are between 0.35-0.71. Nineteen bins have $CC_{3,2} \geq 0.90$ and most of the time delays are positive values, except bin 1 from event #010428. S4KS and S5KS are more difficult to retrieve and measure. This is reflected in the generally lower CC values and larger measurement scatter than S3KS. Fig. 9 shows an example of bin 4 from the event #141101. All the three CC values are higher than 0.94, indicating good quality measurements. For this bin, the measured time delays are 1.30 s for S3KS, 2.48 s for S4KS and 2.59 s for S5KS. The median epicentral distance of this bin is 145.29° and those time delays would indicate a slower Vp than in PREM in the topmost outer core, consistent with previous studies (e.g. Eaton & Kendall, 2006; Helffrich & Kaneshima, 2010; Kaneshima & Helffrich, 2013).

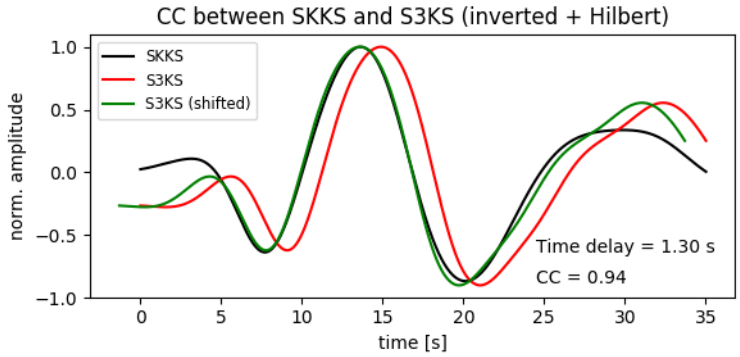

(a)

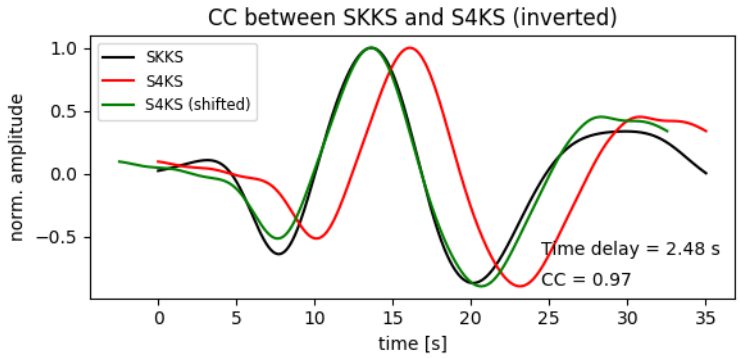

(b)

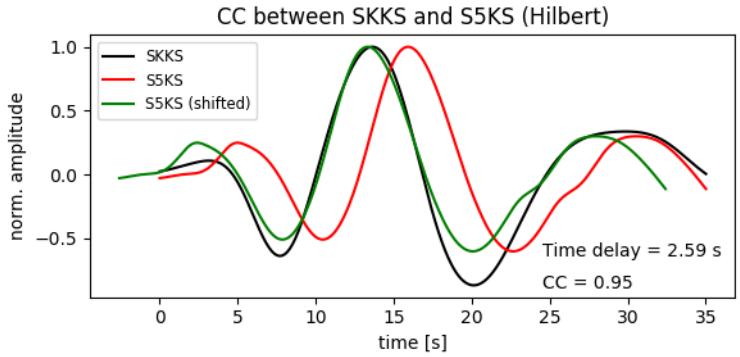

(c)

Figure 9: Time delays of S3KS, S4KS and S5KS measured on bin 4 data after five iterations from event #141101 (0.05-0.2 Hz). (a) CC between SKKS and S3KS (after Hilbert transform and polarity inverted). The black line is the stacked SKKS and the red line represents the stacked S3KS. The green line shows the shifted S3KS with the maximum CC value. The time shift between the red line and green line is 1.30 s and the corresponding CC value is 0.94. Note that the time delay is relative to S3KS-SKKS differential arrival time predicted by PREM. (b) CC between SKKS and S4KS (polarity inverted). (c) CC between SKKS and S5KS (after Hilbert transform).

The measurement qualities are primarily indicated by their CC coefficients. In addition to CC coefficients, amplitude information is also useful to assess the measurement quality. If other factors, such as source radiation pattern, are the same, the amplitude of the SmKS phase decreases with its order m, due to the energy loss at each reflection on the underside of the CMB. All the measurements with good quality at 0.05-0.2 Hz follow this trend of $A_{3,2} > A_{4,2} > A_{5,2}$ (amplitude information in Table S1 and the good quality measurements are listed in Tables S2,S3 and S4).

4.2 3D mantle structure corrections

We run SPECFEM3D_globe to obtain the synthetic seismograms corresponding to the data with good quality measurements. Here, good quality means that more than ten traces are used in a bin and $CC_{3,2} > 0.90$ (Table S1). Most source parameters used in the SEM simulations are from GCMT, but the source durations are replaced with our estimated values. Then we apply our iterative method to these synthetic seismograms to obtain the time delays, amplitude ratios and corresponding CC values. For most bins, we successfully retrieve signals of S3KS, S4KS and S5KS and get high CC coefficients (Table S2). For example, Fig. S5 shows the measurements using synthetic seismograms corresponding to the bin 4 from the event #141101. The CC coefficients are 0.95 for S3KS, 0.96 for S4KS and 0.94 for S5KS, indicating good measurement quality. The S3KS time delay, $3dM_{3,2}^{SEM}$, is as large as 0.60 s and the S4KS time delay, $dt_{4,2}^{SEM}$, is even larger, 1.13 s. The time delays measured on the data are 1.30 s for S3KS and 2.48 s for S4KS (Table S1). Thus, 3D mantle structure corrections are large, up to nearly half the size of the observations, and can not be ignored for this bin. The S3KS measurements on synthetic seismograms of other bins are listed in Table S2 and almost all the bins have $CC_{3,2}^{SEM}$ higher than 0.95, except the bin 1 from #010428 and bin 1 from #140721. The S3KS/SKKS amplitude ratios range from 0.30 to 0.51 and the corrections to S3KS time delays are between -0.95 s and 0.04 s. Most of the corrections have negative values, indicating that S3KS are delayed more than SKKS by the 3D mantle structure. The results for S4KS and S5KS are listed in Tables S3 and S4.

We also use ray theory to compute 3D mantle structure corrections for data at individual stations in each bin and take the average value to represent the correction for that bin. These corrections are close to that measured on SEM synthetic seismograms (Tables S2, S3, S4 and Fig. S6). However, large discrepancies are present for some bins.

For example, the correction to S3KS time delay based on ray theory is 0.27 s for the bin 5 from #141101, but it is -0.22 s using SEM synthetic seismograms.

Fig. 10 shows the SmKS (m=3, 4 and 5) time delays measured on the data with high CC coefficients and the results after 3D mantle structure corrections. Here, we require $CC_{3,2} \geq 0.90$ for a good quality of S3KS measurement. For S4KS, we only take the bins with $CC_{4,2} \geq 0.85$ and $CC_{3,2} \geq 0.90$, because a good quality of S4KS measurement relies on a well-retrieved S3KS. Similarly, we require $CC_{3,2} \geq 0.90$, $CC_{4,2} \geq 0.85$ and $CC_{5,2} \geq 0.80$ for good quality of S5KS measurements.

Most of the bins with good qualities of $dt_{3,2}$ measurements have uncertainties smaller than 0.4 s (Table S2). It is not surprising that $dt_{4,2}$ and $dt_{5,2}$ generally show larger uncertainties than $dt_{3,2}$, due to their smaller SNR and/or incomplete separation of SmKS (m=2, 3, 4 and 5) waveforms of our method. In spite of this, the uncertainties are still much smaller than the anomalies (Tables S4 and S5), because the bins with large errors, resulted from poor phase stripping and/or low SNRs, are discarded by the CC requirements. We note that bootstrapping results only help us infer variance in the dataset, but not able to estimate systematic bias. The systematic bias could be due to strong mantle heterogeneities and source complexities etc, which can be assessed by investigating global data from earthquakes at various places.

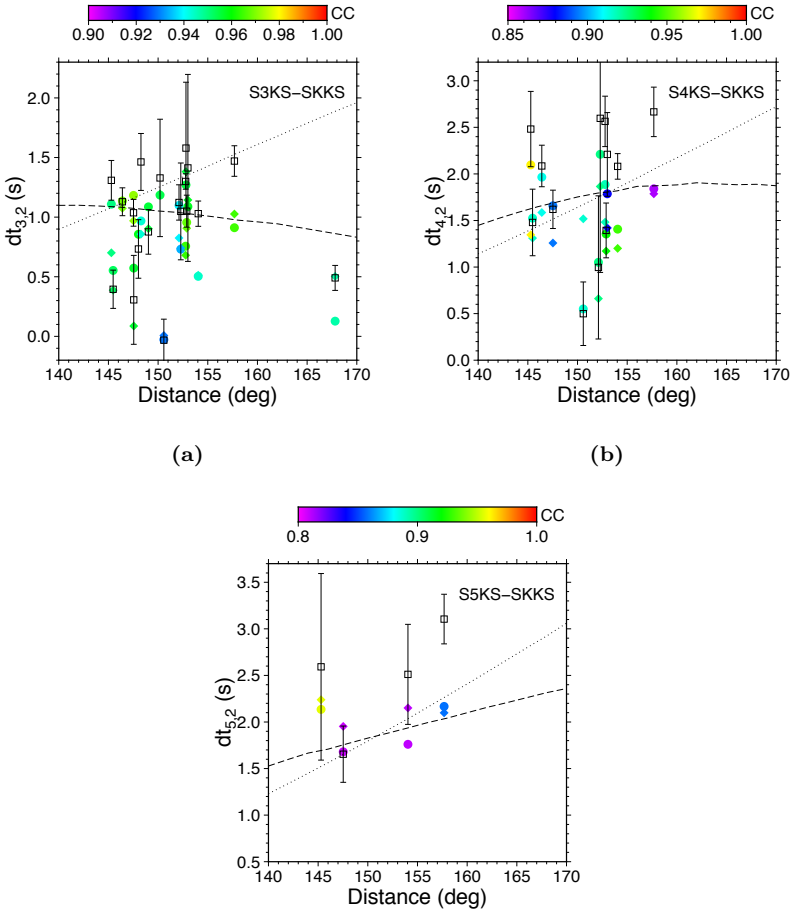

Figure 10: SmKS time delays measured at 0.05-0.2 Hz. The empty squares represent the SmKS (m=3 in a, 4 in b and 5 in c) time delays measured on the data. Note that error bars are symmetric and in a few cases extend beyond the limits of the figure. The solid circles are SmKS time delays after the 3D mantle structure corrections based on ray theory and using S40RTS model. The time delays are relative to SmKS-SKKS differential arrival times predicted by PREM. The solid diamonds are SmKS time delays after the corrections measured on the SEM synthetic seismograms made using S40RTS. The color shows the corresponding CC values measured on the data. More detailed information is displayed in Tables S3-5. The black dashed line in each figure is the corresponding SmKS time delay predicted by KHOMC (Kaneshima & Helffrich, 2013). The black dotted lines show the EPOC predictions. The source depth used in the KHMOC and EPOC predictions is 150 km. (a) S3KS time delays. (b) S4KS time delays. (c) S5KS time delays.

4.3 Comparison between observations and predictions of two 1D models, EPOC and KHOMC

From Fig. 10, we can see that S3KS, S4KS and S5KS time delays predicted by EPOC (Irving et al., 2018) and KHOMC (Kaneshima & Helffrich, 2013) are close to each other at distance $140°-155°$, where most of our data are located. The measured S3KS time delays are generally positive and consistent with the KHOMC and EPOC predictions supporting a slower Vp in the top outer core. The 3D mantle structure corrections, using either ray theory or SEM synthetic seismograms, are primarily negative and therefore reduce the measured S3KS time delays. After the corrections, travel time anomalies are less than the EPOC predictions and they seem to fit the KHOMC predictions better than that of EPOC. The difference between these two models can be better resolved using data at distances $> 160°$, where their difference is larger than 0.5 s. Unfortunately, we have only one such datum, at a distance of 167.8°, so we can not clearly distinguish between EPOC and KHOMC. For S4KS and S5KS, the 3D mantle structure corrections are also primarily negative and they make measurements closer to the KHOMC and EPOC predictions. However, there are a few measurements dramatically departing from the EPOC and KHOMC predictions. For example, $dt^{SEM}_{4,2}$ of bin 1 from #140721 is -0.22 s while the EPOC prediction is 1.22 s. For this bin, the two types of 3D mantle structure corrections have a large difference, 0.12 s from ray theory computation and -0.95 s from SEM synthetic seismograms. This large difference could be due to the limitation of ray theory, uncertainty in the S40RTS model, or poor performance of our method on the synthetic seismograms of this bin. The $CC^{SEM}_{3,2}$ is only 0.91, much lower than that of other bins, which indicates a poor measurement quality. However, $CC_{3,2}$ from data is a high value of 0.96 and its $dt^{ray}_{3,2}$ is close to the EPOC and KHMOC predictions. This big difference is most likely due to a large uncertainty in the 3D mantle corrections using SEM synthetic seismograms. Some other bins, including S3KS time delays of bin 1 from #010428 and S5KS time delays of bin 1 from #010516, have similar issues. Note that the S5KS time delay of bin 1 from #010516 is beyond the y-axis range and not plotted in Fig. 10c.

We also apply two other filters, 0.05-0.7 Hz and 0.1-0.7 Hz, to the data and repeat the measurements. Because running SPECFEM3D_globe to resolve a frequency of 0.7 Hz is very computationally expensive, we only compute the 3D mantle structure corrections using ray theory. Similar to the results at 0.05-0.2 Hz, the S3KS, S4KS and S5KS

measurements at 0.05-0.7 Hz are close to the EPOC and KHMOC predictions after the 3D mantle structure corrections (see Fig. S7).

Note that the bins shown in Fig. S7 are not the same as 0.05-0.7 Hz, because the SNRs of data may change with frequency band and the measurement qualities could also be different. Comparing to 0.05-0.2 Hz and 0.05-0.7 Hz, the number of bins with good measurement qualities is lower at 0.1-0.7 Hz, indicating lower SNRs of data and/or reduced performance of our iterative method for this high frequency band for the data used here. Relatively long period SmKS waves have been stacked to investigate outermost core structure (e.g. 0.02-0.1 Hz in Tanaka, 2007). Shorter period waves have the potential to resolve finer seismic structure. However, source rupture processes and propagation effects due to lateral heterogeneities could give rise to more waveform complexities at shorter period waves reducing the waveform coherencies of SmKS phases and therefore affecting measurement qualities. This might explain the lower number of good quality measurements (Figs. S7d-f) at 0.1-0.7 Hz than that at 0.05-0.2 Hz (Fig. 10) and 0.05-0.7 Hz (Figs. S7a-c).

5 Discussion

SmKS differential arrival times are sensitive to the outer core structure, but accurate measurements of differential arrival times are hampered by their mixed waveforms as a whispering-gallery mode. To extract each individual SmKS phase, Eaton & Kendall (2006) use SKKS as reference waveform and apply deconvolution to SmKS series to convert their waveforms into simple pulses. However, the deconvolution method either requires very high SNR and or has reduced resolution. Here, we develop an iterative method to isolate individual SmKS waveforms with a high resolution. Our method keeps waveform features of each SmKS and therefore allows us to measure SmKS time delays by CC.

We use two different methods, ray theory and SEM synthetic seismograms, to compute effects of mantle heterogeneities and make these corrections to the measurements. The corrections are between -0.5 s and 0.5 s for most bins, but some bins have 3D mantle perturbations even greater than 1.0 s. Furthermore, we see big differences between the two types of corrections for some data (e.g. $>$ 1 s for bin 1 from event #140721), although they generally have positive correlation (Fig. S6). We also used another 3D man-

tle model S362ANI (Kustowski et al., 2008) to compute the SEM synthetic seismograms and measure the 3D mantle structure corrections. Compared to our results using S40RTS, the corrections to S3KS-SKKS, S4KS-SKKS and S5KS-SKKS differential arrival times using S362ANI are generally stronger. Consequently, the corrected SmKS-SKKS (m=3, 4 and 5) time delays become even smaller (Fig. S8,9). Helffrich & Kaneshima (2013) used earthquakes in Fiji and Argentina to investigate SmKS-SKKS time delays. Their measured S3KS-SKKS time delays from Fiji are generally larger than that from Argentina. The earthquakes in our study are geographically close to Fiji and the 3D mantle corrections to S3KS-SKKS time delays tend to reduce the S3KS-SKKS time delays (Fig. 10a). Thus, the higher S3KS-SKKS time delays from events in Fiji by (Helffrich & Kaneshima, 2013) can be largely explained with the 3D mantle structure. 3D mantle structure corrections should be routinely considered to reduce bias in the Vp estimation of uppermost outer core.

After correcting for 3D mantle structure, there are still significant SmKS-SKKS time delays at all of the three frequency bands (Figs. 10 and S7), indicating a lower Vp than PREM model in the shallow outer core. Strong locally concentrated heterogeneities, such as the previously detected Ultra Low Velocity Zones (ULVZs) at the source side of our study region (see, for example, the compilations by S. Yu & Garnero, 2018), are not accurately represented in the smooth global tomography model of S40RTS and could affect the measurements. However, these ULVZ effects have been investigated by Tanaka (2007) and they are expected to be smaller than our measured time delays. In addition, such strong heterogeneities would decrease the coherencies between SKKS and SmKS (m=3, 4 and 5) and only the results with high CC values are selected in our method. Further quantitative investigations will rely on better constraints on the properties and geographical distributions of ULVZ and more detailed numerical waveform modeling. Thus, we do not believe that the SmKS-SKKS travel time delays are solely due to ULVZs, but do indeed indicate a seismically slow uppermost outer core.

Although scatter and uncertainty are present, our measurements are generally consistent with the predictions by the KHOMC and EPOC models. Assuming the outer core is homogeneous, Irving et al. (2018) use a physically consistent equation-of-state (EoS) to parameterize the elastic properties of outer and carry out inversions for seismic normal mode data. This normal mode derived EPOC model shows lower Vp and higher density than PREM at the top of outer core. Although EPOC does not use body-wave data,

its fit to SmKS data is better than PREM (see Fig. 3 in Irving et al. (2018) and Figs. 10 and S7 in this study). KHOMC is derived from SmKS body-wave travel time anomalies and has higher depth resolution than EPOC. We note that both EPOC and KHOMC models have a low Vp at the top of outer core, but they have different depth gradients of Vp. KHOMC seems to fit our results better than EPOC. For example, EPOC over-predicts most S3KS-SKKS time delays after 3D mantle corrections. However, given the scatter present in our measurements, either EPOC or KHOMC fits the data well. The contrast between stratified or homogeneous structure has important implications for understanding the thermochemical status of core and the associated geodynamo. A stratified outer core would change the flow in the outer core and therefore affect the secular variation of geomagnetic field (e.g. Braginsky, 1993; Buffett, 2014; Buffett et al., 2016). However, the detailed effects of such stratification on the geodynamo and the compatibility between seismic and geomagnetic observations (e.g. the thickness of stratified layer) are still inconclusive (Gubbins, 2007; Buffett, 2014; Chulliat & Maus, 2014; Lesur et al., 2015). Additionally, the mechanism for the formation of stratification is also under debate. For example, high concentrations of light elements, including S, O, Si, C and H, at the top of outer core could cause a stratification (e.g. Fearn & Loper, 1981; Buffett & Seagle, 2010; Gubbins & Davies, 2013; Nakagawa, 2018; Helffrich & Kaneshima, 2013), but how these light elements change Vp is still under debate (Helffrich, 2012; Brodholt & Badro, 2017). In this study, we cannot easily distinguish between the EPOC and KHOMC models, but these two models do give different predictions of SmKS-SKKS differential arrival times. Thus, both gathering more observations, e.g. S3KS-SKKS differential times at a distance$> 160°$, and considering other geophysical probes of the outer core, for example normal mode observations, will be critical to better resolve the uppermost outer core's density and Vp, providing vital data to constrain the thermochemical status of the outer core.

6 Conclusions

We introduce an array-based iterative method to measure SmKS-SKKS (m=3, 4 and 5) differential arrival times and use them to investigate the Vp in Earth's uppermost outer core. We validate this method by testing synthetic seismograms and apply this method to data at stations in Europe from eleven earthquakes in Fiji-Tonga, Vanuatu, New Britain and Solomon Islands. Using the SKKS signal as a reference, S3KS, S4KS and S5KS wave-

forms are successfully extracted and S3KS-SKKS, S4KS-SKKS and S5KS-SKKS differential arrival times are measured by waveform cross-correlation. This iterative method not only gives us the measurements of differential arrival times, but also allow us to assess measurement qualities based the CC coefficients and amplitude information. SmKS-SKKS differential arrival times are sensitive to Vp at the top of the outer core, but 3D mantle structures could also affect the arrival times. We use the 3D mantle model S40RTS and two different methods, ray theory and SEM synthetic seismograms, to estimate these anomalies for the frequency of 0.05-0.2 Hz. The results show that the arrival time anomalies due to 3D mantle structure effects are large (e.g. > 0.5 s) for some data and sometimes there are big differences between the corrections calculated using ray theory and SEM synthetics. After corrections for 3D mantle structure, we still see large positive S3KS-SKKS, S4KS-SKKS and S5KS-SKKS differential arrival times, indicating a lower Vp than in PREM at the top of outer core. Our measurements are consistent with the predictions of KHOMC and EPOC models. EPOC has a homogeneous outer core while KHOMC contains a stratified layer at the top of outer core. Based on the data in this study, we cannot clearly distinguish the KHOMC and EPOC models, so more data, e.g. S3KS-SKKS differential time at a distances $> 160°$, will be necessary to help us distinguish between them.

Acknowledgments

We acknowledge support from the NSF (EAR1644399 and 1736046). The authors thank J. Ristema and C.A. Moreno Chaves for their code to calculate ray theoretical times through S40RTS. The authors acknowledge the use of the GMT (Wessel & Smith, 1998) and SAC (Goldstein et al., 2003) software packages. We acknowledge support from the NSF (EAR1644399 and 1736046). Waveform data (from a range of networks detailed in the References) have been collected using the Python toolbox ObsPy (Beyreuther et al., 2010).

References

Alexandrakis, C., & Eaton, D. W. (2007). Empirical transfer functions: Application to determination of outermost core velocity structure using SmKS phases. *Geophys. Res. Lett.*, *34*, L22317. doi: 10.1029/2007gl031932

Alexandrakis, C., & Eaton, D. W. (2010). Precise seismic-wave velocity atop Earth's

core: No evidence for outer-core stratification. *Phys. Earth Planet. Inter.*, *180*(1-2), 59–65. doi: 10.1016/j.pepi.2010.02.011

Beyreuther, M., Barsch, R., Krischer, L., Megies, T., Behr, Y., & Wassermann, J. (2010). ObsPy: A Python Toolbox for Seismology. *Seismol. Res. Lett.*, *81*(3), 530–533. doi: 10.1785/gssrl.81.3.530

Braginsky, S. I. (1993). MAC-Oscillations of the Hidden Ocean of the Core. *J. Geomagn. Geoelectr.*, *45*(11), 1517–1538. doi: 10.5636/jgg.45.1517

Brodholt, J., & Badro, J. (2017). Composition of the low seismic velocity E′ layer at the top of Earth's core. *Geophys. Res. Lett.*, *44*(16), 8303–8310. doi: 10.1002/2017GL074261

Buffett, B. (2014). Geomagnetic fluctuations reveal stable stratification at the top of the Earth's core. *Nature*, *507*(7493), 484–487. doi: 10.1038/nature13122

Buffett, B., Knezek, N., & Holme, R. (2016). Evidence for MAC waves at the top of Earth's core and implications for variations in length of day. *Geophys. J. Int.*, *204*(3), 1789–1800. doi: 10.1093/gji/ggv552

Buffett, B., & Seagle, C. (2010). Stratification of the top of the core due to chemical interactions with the mantle. *J. Geophys. Res.*, *115*, B04407. doi: 10.1029/2009jb006751

Choy, G. L. (1977). Theoretical seismograms of core phases calculated by frequency-dependent full wave theory, and their interpretation. *Geophys. J. Int.*, *51*(2), 275–312. doi: 10.1111/j.1365-246x.1977.tb06921.x

Choy, G. L., & Richards, P. G. (1975). Pulse distortion and hilbert transformation in multiply reflected and refracted body waves. *Bull. Seismol. Soc. Am.*, *65*(1), 55–70.

Chulliat, A., & Maus, S. (2014). Geomagnetic secular acceleration, jerks, and a localized standing wave at the core surface from 2000 to 2010. *J. Geophys. Res.*, *119*(3), 1531–1543. doi: 10.1002/2013JB010604

Dziewonski, A. M., & Anderson, D. L. (1981). Preliminary reference Earth model. *Phys. Earth Planet. Inter.*, *25*(4), 297–356. doi: 10.1016/0031-9201(81)90046-7

Eaton, D. W., & Kendall, J.-M. (2006). Improving seismic resolution of outermost core structure by multichannel analysis and deconvolution of broadband SmKS phases. *Phys. Earth Planet. Inter.*, *155*(1-2), 104–119. doi: 10.1016/j.pepi.2005.10.007

Efron, B., & Tibshirani, R. (1991, jul). Statistical Data Analysis in the Computer Age. *Science*, *253*(5018), 390–395. doi: 10.1126/science.253.5018.390

Ekström, G., Nettles, M., & Dziewoński, A. (2012). The global CMT project 2004–2010: Centroid-moment tensors for 13,017 earthquakes. *Phys. Earth Planet. Inter.*, *200-201*, 1–9. doi: 10.1016/j.pepi.2012.04.002

Fearn, D. R., & Loper, D. E. (1981). Compositional convection and stratification of Earth's core. *Nature*, *289*(5796), 393. doi: 10.1038/289393a0

Garnero, E. J., & Helmberger, D. V. (1995). On seismic resolution of lateral heterogeneity in the Earth's outermost core. *Phys. Earth Planet. Inter.*, *88*(2), 117–130. doi: 10.1016/0031-9201(94)02976-i

Garnero, E. J., Helmberger, D. V., & Engen, G. (1988). Lateral variations near the core-mantle boundary. *Geophys. Res. Lett.*, *15*(6), 609–612. doi: 10.1029/gl015i006p00609

Garnero, E. J., Helmberger, D. V., & Grand, S. P. (1993). Constraining outermost core velocity with SmKS waves. *Geophys. Res. Lett.*, *20*(22), 2463–2466. doi: 10.1029/93gl02823

Garnero, E. J., McNamara, A. K., & Shim, S.-H. (2016). Continent-sized anomalous zones with low seismic velocity at the base of Earth's mantle. *Nat. Geosci.*, *9*(7), 481–489. doi: 10.1038/ngeo2733

Goldstein, P., Dodge, D., Firpo, M., & Minner, L. (2003). SAC2000: Signal processing and analysis tools for seismologists and engineers. *The IASPEI International Handbook of Earthquake and Engineering Seismology*, *81*, 1613–1620.

Gubbins, D. (2007). Geomagnetic constraints on stratification at the top of Earth's core. *Earth Planets Space*, *59*(7), 661–664. doi: 10.1186/bf03352728

Gubbins, D., & Davies, C. (2013). The stratified layer at the core-mantle boundary caused by barodiffusion of oxygen, sulphur and silicon. *Phys. Earth Planet. Inter.*, *215*, 21–28. doi: 10.1016/j.pepi.2012.11.001

Hales, A., & Roberts, J. (1971). The velocities in the outer core. *Bull. Seismol. Soc. Am.*, *61*(4), 1051–1059.

Helffrich, G. (2012). How light element addition can lower core liquid wave speeds. *Geophys. J. Int.*, *188*(3), 1065–1070. doi: 10.1111/j.1365-246x.2011.05295.x

Helffrich, G., & Kaneshima, S. (2010). Outer-core compositional stratification from observed core wave speed profiles. *Nature*, *468*(7325), 807–810. doi: 10.1038/

765 nature09636

766 Helffrich, G., & Kaneshima, S. (2013). Causes and consequences of outer core strati-
767 fication. *Phys. Earth Planet. Inter.*, *223*, 2–7. doi: 10.1016/j.pepi.2013.07.005

768 Hirose, K., Labrosse, S., & Hernlund, J. (2013). Composition and state of the core.
769 *Annu. Rev. Earth Planet. Sci.*, *41*, 657–691. doi: 10.1146/annurev-earth-050212
770 -124007

771 Irving, J. C. E., Cottaar, S., & Lekić, V. (2018). Seismically determined elastic pa-
772 rameters for Earth's outer core. *Sci. Adv.*, *4*(6), eaar2538. doi: 10.1126/sciadv
773 .aar2538

774 Kaneshima, S. (2018). Array analyses of SmKS waves and the stratification
775 of earth's outermost core. *Phys. Earth Planet. Inter.*, *276*, 234–246. doi:
776 10.1016/j.pepi.2017.03.006

777 Kaneshima, S., & Helffrich, G. (2013). Vp structure of the outermost core derived
778 from analysing large-scale array data of SmKS waves. *Geophys. J. Int.*, *193*(3),
779 1537–1555. doi: 10.1093/gji/ggt042

780 Kaneshima, S., & Matsuzawa, T. (2015). Stratification of Earth's outermost core in-
781 ferred from SmKS array data. *Prog Earth Planet Sci*, *2*(1). doi: 10.1186/s40645
782 -015-0046-5

783 Komatitsch, D., & Tromp, J. (1999). Introduction to the spectral element method
784 for three-dimensional seismic wave propagation. *Geophys. J. Int.*, *139*(3), 806–822.
785 doi: 10.1046/j.1365-246x.1999.00967.x

786 Komatitsch, D., & Tromp, J. (2002). Spectral-element simulations of global seis-
787 mic wave propagation-II. three-dimensional models, oceans, rotation and self-
788 gravitation. *Geophys. J. Int.*, *150*(1), 303–318. doi: 10.1046/j.1365-246x.2002
789 .01716.x

790 Kustowski, B., Ekström, G., & Dziewoński, A. (2008). Anisotropic shear-wave ve-
791 locity structure of the Earth's mantle: A global model. *J. Geophys. Res.*, *113*(B6).
792 doi: 10.1029/2007jb005169

793 Lesur, V., Whaler, K., & Wardinski, I. (2015). Are geomagnetic data consistent with
794 stably stratified flow at the core-mantle boundary? *Geophys. J. Int.*, *201*(2), 929–
795 946. doi: 10.1093/gji/ggv031

796 Luo, Y., Tromp, J., Denel, B., & Calandra, H. (2013). 3D coupled acoustic-elastic
797 migration with topography and bathymetry based on spectral-element and adjoint

methods. *Geophysics*, *78*(4), S193–S202. doi: 10.1190/geo2012-0462.1

Nakagawa, T. (2018). On the thermo-chemical origin of the stratified region at the top of the Earth's core. *Phys. Earth Planet. Inter.*, *276*, 172–181. doi: 10.1016/j.pepi.2017.05.011

Ohtaki, T., & Kaneshima, S. (2015). Independent estimate of velocity structure of Earth's lowermost outer core beneath the northeast Pacific from PKiKP- PKPbc differential traveltime and dispersion in PKPbc. *J. Geophys. Res.*, *120*(11), 7572–7586. doi: 10.1002/2015jb012140

Ritsema, J., Deuss, A., van Heijst, H. J., & Woodhouse, J. H. (2011). S40RTS: a degree-40 shear-velocity model for the mantle from new Rayleigh wave dispersion, teleseismic traveltime and normal-mode splitting function measurements. *Geophys. J. Int.*, *184*(3), 1223–1236. doi: 10.1111/j.1365-246x.2010.04884.x

Song, X., & Helmberger, D. V. (1995). A P-wave velocity model of Earth's core. *J. Geophys. Res.*, *100*(B6), 9817–9830. doi: 10.1029/94JB03135

Souriau, A., & Poupinet, G. (1991a). A study of the outermost liquid core using differential travel times of the SKS, SKKS and S3KS phases. *Phys. Earth Planet. Inter.*, *68*(1-2), 183–199. doi: 10.1016/0031-9201(91)90017-c

Souriau, A., & Poupinet, G. (1991b). The velocity profile at the base of the liquid core from PKP(BC+Cdiff) data: An argument in favour of radial inhomogeneity. *Geophys. Res. Lett.*, *18*(11), 2023–2026. doi: 10.1029/91gl02417

Stevenson, D. (1987). Limits on lateral density and velocity variations in the Earth's outer core. *Geophys. J. Int.*, *88*(1), 311–319. doi: 10.1111/j.1365-246x.1987.tb01383.x

Tanaka, S. (2004). Seismic detectability of anomalous structure at the top of the Earth's outer core with broadband array analysis of SmKS phases. *Phys. Earth Planet. Inter.*, *141*(3), 141–152. doi: 10.1016/j.pepi.2003.11.006

Tanaka, S. (2007). Possibility of a low P-wave velocity layer in the outermost core from global SmKS waveforms. *Earth Planet. Sci. Lett*, *259*(3-4), 486–499. doi: 10.1016/j.epsl.2007.05.007

Tang, V., Zhao, L., & Hung, S.-H. (2015). Seismological evidence for a non-monotonic velocity gradient in the topmost outer core. *Scientific Reports*, *5*(1), 8613. doi: 10.1038/srep08613

Tromp, J., Komatitsch, D., & Liu, Q. (2008). Spectral-element and adjoint methods

in seismology. *Comm. Comput. Phys.*, *3*(1), 1–32.

The waveform data used in this study is from the following networks:

AC, AF (doi:10.7914/SN/AF), BA, BE (doi:10.7914/SN/BE), BL, BN, BS (doi:10.7914/SN/BS), BW (doi:10.7914/SN/BW), C, C1 (doi:10.7914/SN/C1), CA (doi:10.7914/SN/CA), CB (doi:10.7914/SN/CB), CH (doi:10.12686/sed/networks/ch), CM, CN (doi:10.7914/SN/CN), CR, CU (doi:10.7914/SN/CU), CX (doi:10.14470/PK615318), CZ (doi:10.7914/SN/CZ), DK, DR (doi:10.7914/SN/DR), DZ, EB, EE, EI (doi:10.7914/SN/EI), FN, FR (doi:10.15778/RESIF.FR), G (doi:10.18715/GEOSCOPE.G), GB, GE (doi:10.14470/TR560404), GR, GS (doi:10.7914/SN/GS), GT (doi:10.7914/SN/GT), GU (doi:10.7914/SN/GU), HE (doi:10.14470/UR044600), HL (doi:10.7914/SN/HL), HT (doi:10.7914/SN/HT), HU (doi:10.14470/UH028726), IB (doi:10.7914/SN/IB), II(doi:10.7914/SN/II), IM, IP, IS, IU(doi:10.7914/SN/IU), IV (doi:10.13127/SD/X0FXnH7QfY), KC (doi:10.7914/SN/KC), KN, KO (doi:10.7914/SN/KO), KP (doi:10.7914/SN/KP), KR (doi:10.7914/SN/KR), KW, KZ (doi:10.7914/SN/KZ), LD, LI (doi:10.7914/SN/LI), LX, MC, MD (doi:10.7914/SN/MD), MN (doi:10.13127/SD/fBBBtDtd6q), MX (doi:10.21766/SSNMX/SN/MX), N4 (doi:10.7914/SN/N4), NA (doi:10.21944/dffa7a3f-7e3a-3b33-a436-516a01b6af3f), NE (doi:10.7914/SN/NE), NI (doi:10.7914/SN/NI), NJ (doi:10.7914/SN/NJ), NL (doi:10.21944/e970fd34-23b9-3411-b366-e4f72877d2c5), NM, NO, NR (doi:10.7914/SN/NR), NU (doi:10.7914/SN/NU), OE (doi:10.7914/SN/OE), OV, OX (doi:10.7914/SN/OX), PE (doi:10.7914/SN/PE), PL, PM, PR (doi:10.7914/SN/PR), PZ (doi:10.7914/SN/PZ), RD (doi:10.15778/RESIF.RD), RO (doi:10.7914/SN/RO), SI, SJ, SK (doi:10.14470/FX099882), SL (doi:10.7914/SN/SL), SP (doi:10.7914/SN/SP), SS, SV, SX (doi:10.7914/SN/SX), TA (doi:10.7914/SN/TA), TH (doi:10.7914/SN/TH), TR, TT, TU, UK, UP (doi:10.18159/SNSN), US (doi:10.7914/SN/US), VE, VI, WC, WI (doi: doi:10.18715/antilles.WI), WM (doi:10.14470/JZ581150), X5, X6 (doi:10.7914/SN/X6_2007), X7 (doi:10.15778/RESIF.X72010), XB (doi:10.7914/SN/XB_2009), XE (doi:10.7914/SN/XE_2009), XI (doi:10.7914/SN/XI_2011), XJ (doi:10.12686/sed/networks/xh), XK

(doi:10.7914/SN/XK_2012), XN (doi:10.7914/SN/XN_2008), XO (doi:10.7914/SN/XO_2011), XQ (doi:10.7914/SN/XQ_2012), XT (doi:10.7914/SN/XT_2003), XV (doi:10.7914/SN/XV_2011), XW (doi:10.15778/RESIF.XW2007 and doi:10.7914/SN/XW_2009), XY (doi:10.15778/RESIF.XY2007 and doi:10.7914/SN/XY_2010), XZ (doi:10.7914/SN/XZ_2003), Y1, Y4 (doi:10.15778/RESIF.Y42004), YB (doi:10.15778/RESIF.YB2000 and doi:10.7914/SN/YB_2013), YD, YF, YG, YH (doi:10.7914/SN/YH_2012), YI (doi:10.7914/SN/YI_2003 and doi:10.15778/RESIF.YI2008), YJ, YK, YO (doi:10.7914/SN/YO_2014), YP, YQ (doi:10.7914/SN/YQ_2013), YR (doi:10.15778/RESIF.YR1999), YS (doi:10.7914/SN/YS_2009), YV, YW, YY, YZ (doi:10.7914/SN/YZ_2009), Z4 (doi:10.7914/SN/Z4_2009), Z9 (doi:10.7914/SN/Z9_2010), ZA, ZC (doi:10.7914/SN/ZC_2013), ZD (doi:10.7914/SN/ZD_2010), ZE (doi:10.7914/SN/ZE_2007), ZF, ZG (doi:10.7914/SN/ZG_2010), ZH (doi:10.15778/RESIF.ZH2003), ZL (doi:10.7914/SN/ZL_2007), ZN, ZO (doi:10.7914/SN/ZO_2010), ZP, ZR, ZS, ZT (doi:10.7914/SN/ZT_2015), ZU, ZV, ZX, ZZ (doi:10.14470/MM7557265463), 1E, 4F, 6D, 6E, 7A (doi:10.7914/SN/7A_2013), 7C (doi:10.15778/RESIF.7C2009), 7E (doi:10.14470/2R383989), 7J, 8A, 9D (doi:10.7914/SN/9A_2012). (n.d.).

Wessel, P., & Smith, W. H. (1998). New, improved version of Generic Mapping Tools released. *EOS Trans. Amer. Geophys. Union*, *79*(47), 579–579. doi: 10.1029/98EO00426

Yu, S., & Garnero, E. J. (2018). Ultralow Velocity Zone Locations: A Global Assessment. *Geochem. Geophys. Geosyst.*, *19*(2), 396–414. doi: 10.1002/2017gc007281

Yu, Z., Ni, S., Wei, S., Zeng, X., Wu, W., & Li, Z. (2012). An iterative algorithm for separation of S and ScS waves of great earthquakes. *Geophys. J. Int.*, *191*(2), 591–600. doi: 10.1111/j.1365-246x.2012.05603.x

Zou, Z., Koper, K. D., & Cormier, V. F. (2008). The structure of the base of the outer core inferred from seismic waves diffracted around the inner core. *J. Geophys. Res.*, *113*(B5). doi: 10.1029/2007jb005316

Supporting Information for "Array-based iterative measurements of SmKS travel times and their constraints on outermost core structure"

Wenbo, Wu[1,2], and Jessica, C. E. Irving [1]

[1] Department of Geosciences, Princeton University, Princeton, NJ 08541, USA

[2]Seismological Laboratory, Division of Geological and Planetary Sciences, California Institute of Technology, Pasadena, CA 91125, USA

Contents of this file

1. Text S1 to S9
2. Figures S1 to S9
3. Tables S1 to S5

S1. Introduction

This document includes descriptions of the data used in this study, array-data bin formation, source time function estimations and discussion of the effects of 3D mantle structure.

S2. Data used in this study

We collect broadband and short period data at global stations with distances $\geq 120^{\circ}$ from earthquakes in Fiji-Tonga, Vanuatu, New Britain and Solomon Islands (Fig. S1). Global station coverage is highly uneven. For example, data from oceans is scarcest and

continents, especially Europe and North America, are well instrumented. In this study, we mainly focus on the data at stations from Europe. Note that we use the data in Fig. S1 to find the potentially good events, but only data at stations with distances $\geq 140^\circ$ from the event good events are used for the measurements of SmKS-SKKS differential arrival time. At shorter distances, S3KS and SKKS arrival times are too close affecting quality of cut SKKS waveforms.

S3. Waveform cross correlations in synthetic tests

To validate our iterative method, we make synthetic seismograms and measure the SmKS travel time delays. After the first two iterations, SmKS (m=3, 4 and 5) waveforms are successfully retrieved and the time delays are accurately measured (Fig. 7). The high CC coefficients (e.g. waveform cross correlation between SKKS and S5KS in Fig. S2) demonstrate the validation of our method.

S4. Data bin formation

Here we show an example of bin formation. The good SmKS data from the event #141101 are divided into five geographical bins (Fig. S3). The boundaries of each bin are defined at the given distances and azimuths. For example, bin2 is defined with $151^\circ \leq$distance$\leq 163^\circ$ and $337^\circ \leq$azimuth$\leq 360^\circ$. Similarly, the bins are formed for the other ten events with given distances and azimuths.

S5. Estimated source time functions

GCMT does not really make inversions for source duration, so we re-estimate the source durations of the eleven good events. We use the global teleseismic ($30^\circ \leq$ epicentral distance $\leq 95^\circ$) P-waves from networks II and IU to estimate the duration (e.g. Fig. S4). We collect broadband vertical seismograms from II and IU, remove the instrument responses

and convert them to displacement. Then we pick the onsets of direct P-waves, take the clear data and visually check their polarities, inverting these with negative polarities. The waveforms are aligned on their onsets, normalized with peak amplitudes and finally stacked to get an estimated source time function. We use this method to estimate the source time functions of each earthquake.

S6. Waveform cross correlations for the bin4 from the event #141101 We use the CC coefficients to assess measurement quality. For example, the CC coefficients of SmKS-SKKS (m=3, 4 and 5) for the bin4 from the event #141101 are higher than 0.94 (Fig. S5), that indicates a good quality of measurement.

S7. 3D mantle structure corrections derived from ray theory and SEM synthetic seismograms

We use two different methods, ray theory and SEM synthetic seismograms, to compute the 3D mantle effects on the SmKS-SKKS differential arrival times at 0.05-0.2 Hz. Fig. S6 shows the comparison between the two types of corrections for S3KS-SKKS differential arrival times. Generally, these two types of corrections show an expected positive correlation, although some bins have a large discrepancy.

S8. SmKS travel time delays measured at 0.05-0.7 Hz and 0.1-0.7 Hz

In the main text, the SmKS travel time delays are measured at 0.05-0.2 Hz. Here, we measure the SmKS travel time delays at another two frequency bands of 0.05-0.7 Hz and 0.1-0.7 Hz. We use the same parameters as 0.05-0.2 Hz to measure 0.05-0.7 Hz data. For a higher frequency band of 0.1-0.7 Hz, we use a shorter time window of 0-40 s to cut SKKS and cut 25 s waveforms for CC computation. The S3KS, S4KS and S5KS measurements at 0.05-0.7 Hz are similar to those at 0.05-0.2 Hz and close to the EPOC and KHMOC

predictions after the 3D mantle structure corrections (Fig. S7). At 0.1-0.7 Hz, the number of bins with good measurement qualities is reduced, indicating lower SNRs of data and/or reduced performance of our iterative method for this high frequency band for the data used here.

S9. 3D mantle structure corrections using 3D tomography models S40RTS and S362ANI

We use two different 3D mantle models of S40RTS (Ritsema, Deuss, van Heijst, & Woodhouse, 2011) and S362ANI (Kustowski, Ekström, & Dziewoński, 2008) to compute the SEM synthetic seismograms and measure the 3D mantle structure corrections. For simplicity, we choose the option of "s362iso" to implement the S362ANI model in SPECFEM3D_globe. The corrections to S3KS-SKKS differential arrival times of these two models show a generally positive correlation, but the corrections using S40RTS are weaker than that using S362ANI for all bins except one (Fig. S8). Consequently, the S3KS-SKKS time delays after the 3D mantle structure corrections using S40RTS are generally larger than that using S362ANI (Fig. S9a). This difference is also seen in the S4KS-SKKS and S5KS-SKKS differential arrival times (Fig. S9b,c). These results indicate a model dependent 3D mantle structure corrections.

References

Ekström, G., Nettles, M., & Dziewoński, A. (2012). The global CMT project 2004–2010: Centroid-moment tensors for 13,017 earthquakes. *Phys. Earth Planet. Inter.*, *200-201*, 1–9. doi: 10.1016/j.pepi.2012.04.002

Irving, J. C. E., Cottaar, S., & Lekić, V. (2018). Seismically determined elastic parameters for Earth's outer core. *Sci. Adv.*, *4*(6), eaar2538. doi: 10.1126/sciadv.aar2538

Kaneshima, S., & Helffrich, G. (2013). Vp structure of the outermost core derived from analysing large-scale array data of SmKS waves. *Geophys. J. Int.*, *193*(3), 1537–1555. doi: 10.1093/gji/ggt042

Kustowski, B., Ekström, G., & Dziewoński, A. (2008). Anisotropic shear-wave velocity structure of the Earth's mantle: A global model. *J. Geophys. Res.*, *113*(B6). doi: 10.1029/2007jb005169

Ritsema, J., Deuss, A., van Heijst, H. J., & Woodhouse, J. H. (2011). S40RTS: a degree-40 shear-velocity model for the mantle from new Rayleigh wave dispersion, teleseismic traveltime and normal-mode splitting function measurements. *Geophys. J. Int.*, *184*(3), 1223–1236. doi: 10.1111/j.1365-246x.2010.04884.x

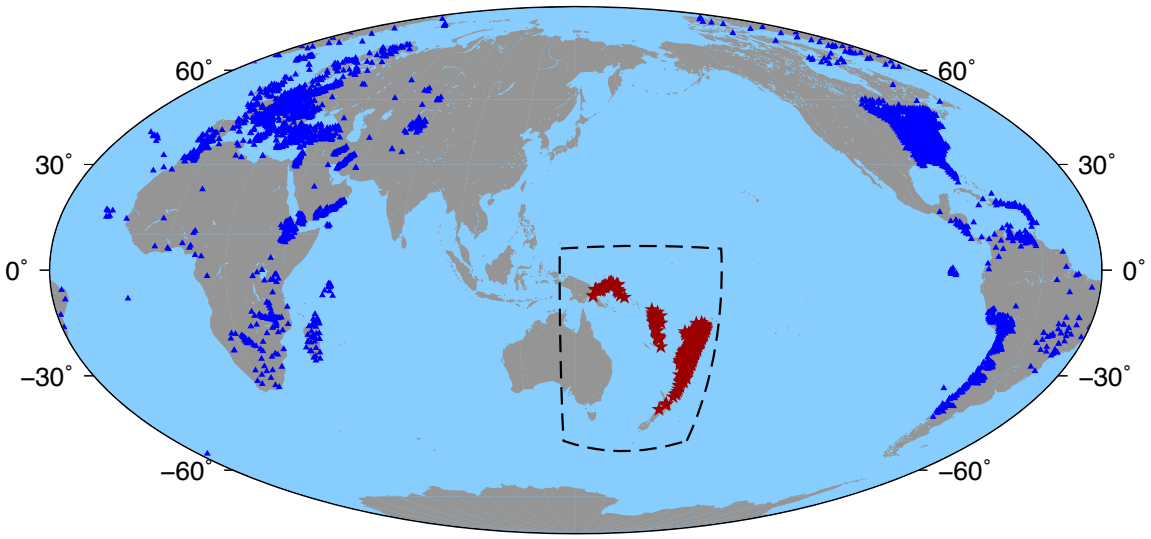

Figure S1. Earthquakes and stations investigated in this study. We collect data at global stations with distances $\geq 120°$ from earthquakes in the black dashed line box. The earthquakes are mainly located in the regions of Fiji-Tonga, Vanuatu, New Britain and Solomon Islands. To get high quality data, we only select earthquakes with depths $\geq$150 km and Mw $\geq$5.5 (Global Centroid-Moment Tensor catalog, Ekström et al., 2012) from the years 2000 to 2016.

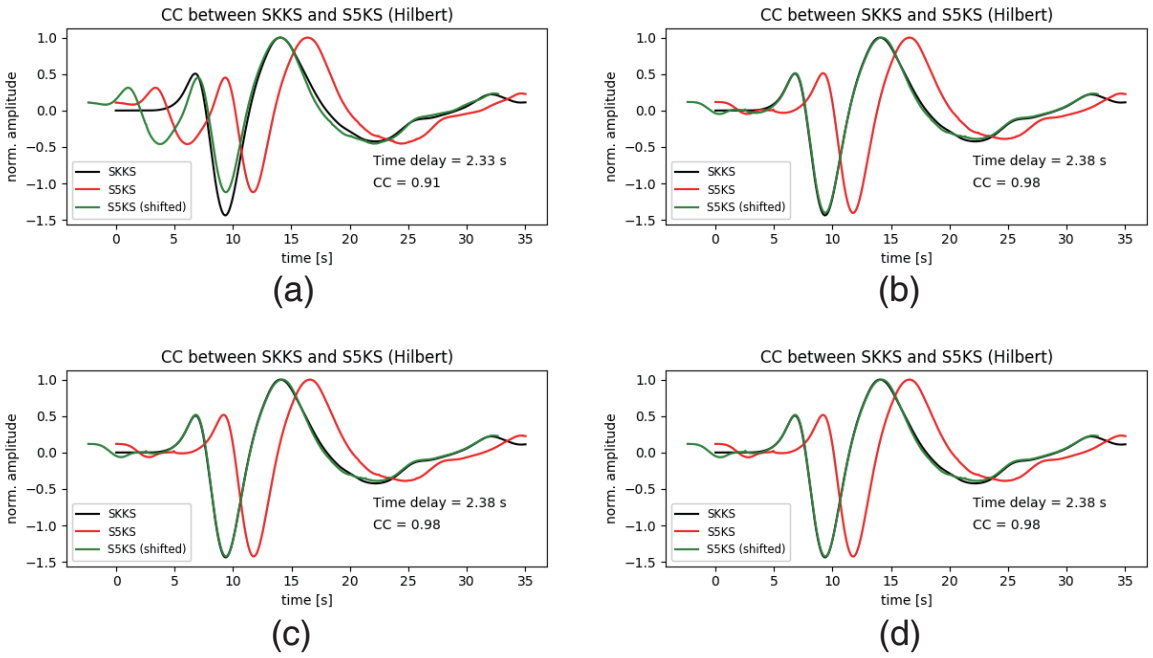

Figure S2. Waveform cross correlation between SKKS and S5KS (after Hilbert transform) in the first four iterations. The black lines are the stacked SKKS and the red lines show the stacked S5KS. The green lines are shifted S5KS with the maximum CC values. The measured time delay is 2.33 s in the first iteration and 2.38 s in the next three iterations, which is close to the input 2.39 s. The time delays are relative to SmKS-SKKS differential arrival times predicted by PREM.

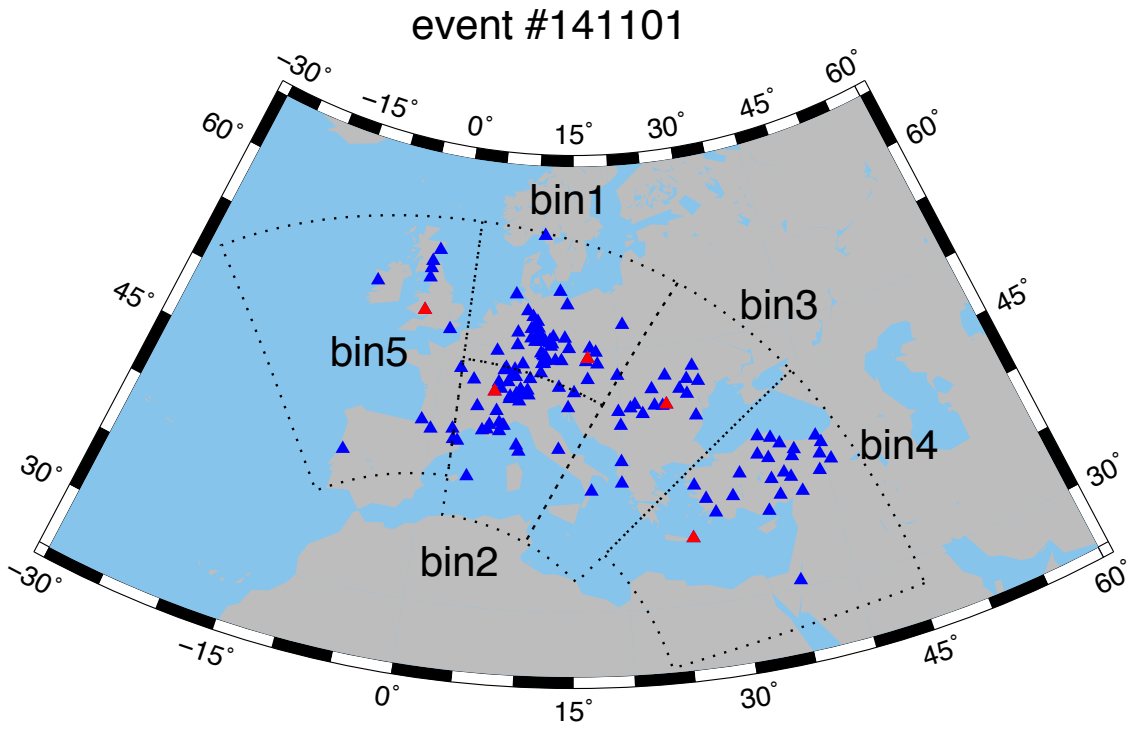

Figure S3. A map of five bins used for event #141101. The blue triangles are the stations used to measure the SmKS-SKKS (m=3, 4 and 5) differential arrival times. The red triangles show the five reference stations used to align the SKKS waveforms.

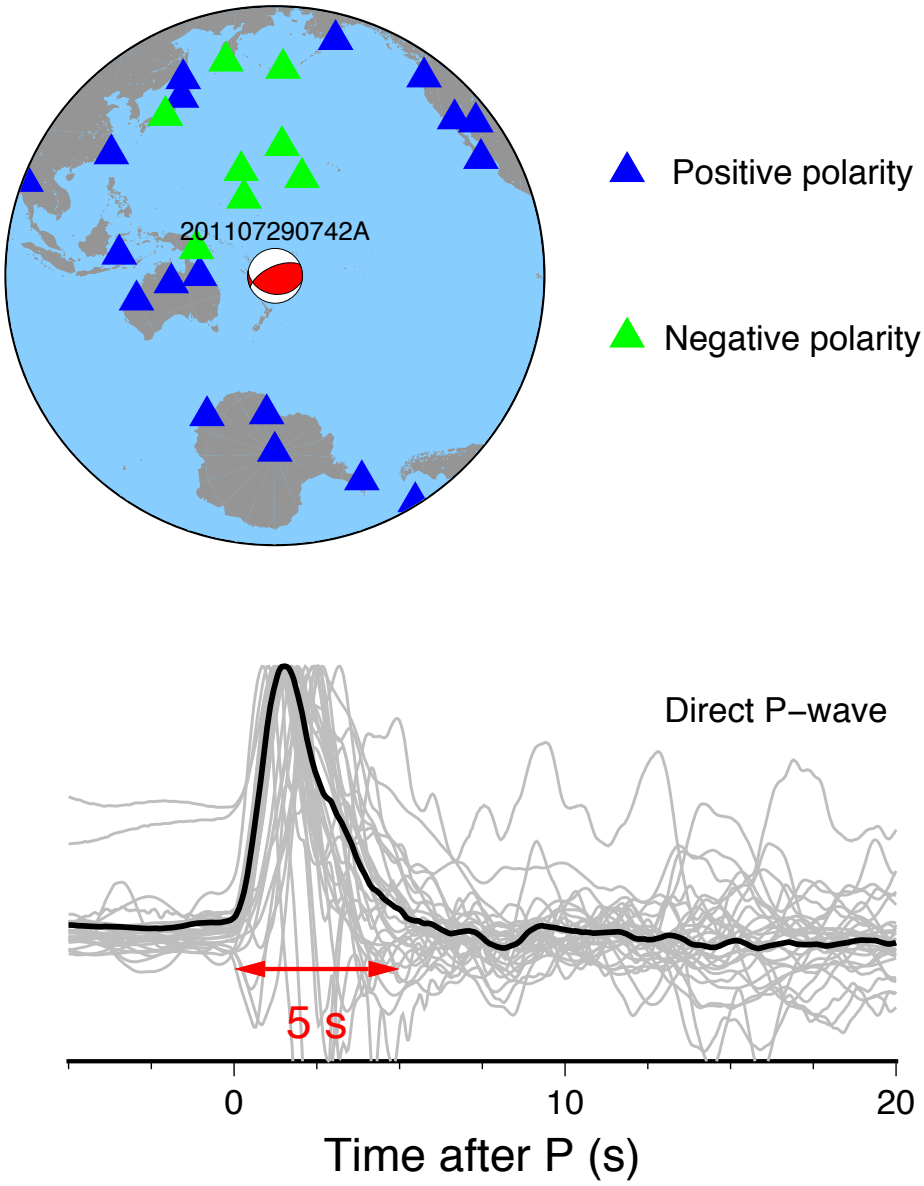

Figure S4. Estimated source time function of event #110729. The upper map shows the teleseismic stations used to estimate the source time function. The blue triangles represent the stations with positive polarities of direct P-wave and the green ones have negative polarities. The beach ball shows the GCMT solution for this earthquake. The lower figure shows the corresponding direct P-waves. The gray lines are waveforms at stations in the upper map (negative polarities are inverted) and the black line is the stacked waveform. Time zero is the hand-picked onsets of each direct P-waves. The red arrow illustrates the estimated source duration of about 5 s.

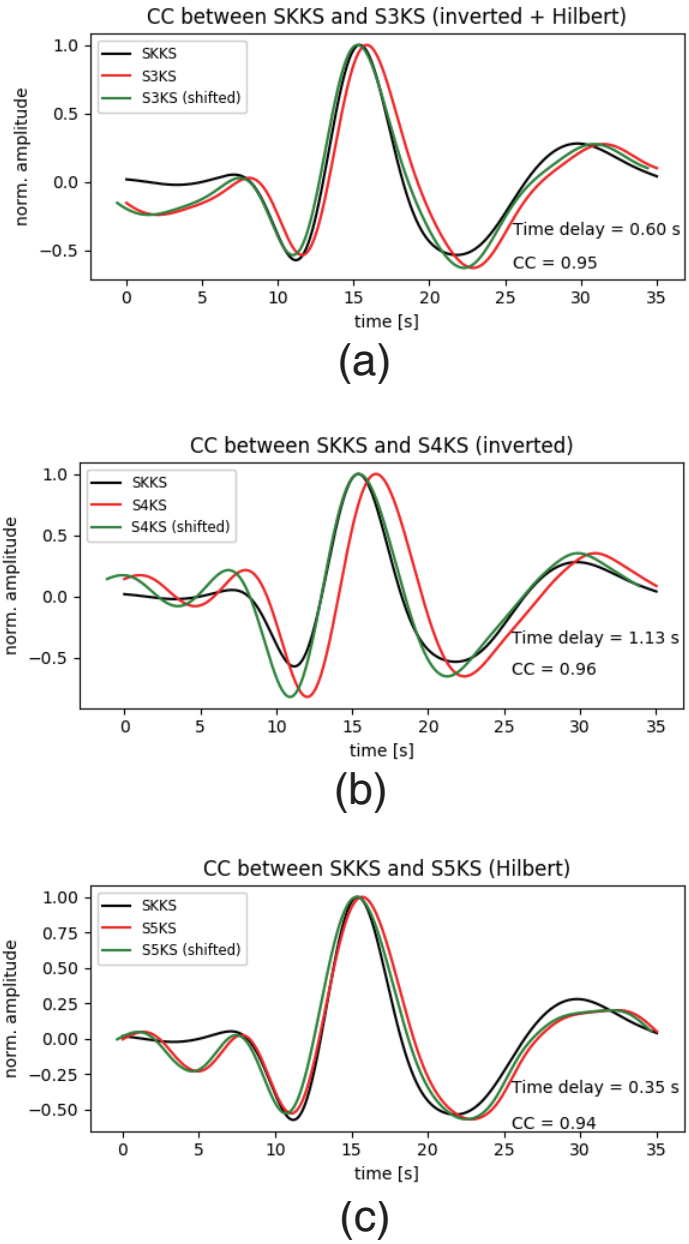

Figure S5. SmKS (m=3, 4 and 5) time delays measured on the SEM synthetics corresponding to the bin 4 from the event #141101. The time delays are relative to SmKS-SKKS differential arrival times predicted by PREM. (a) CC between SKKS and S3KS (after Hilbert transform and polarity inverted). The black line is the stacked SKKS and the red line represents the stacked S3KS. The green line shows the shifted S3KS with the maximum CC value. The time shift between the red line and green line is 0.60 s and the corresponding CC value is 0.95. (b) CC between SKKS and S4KS (polarity inverted). (c) CC between SKKS and S5KS (after Hilbert transform).

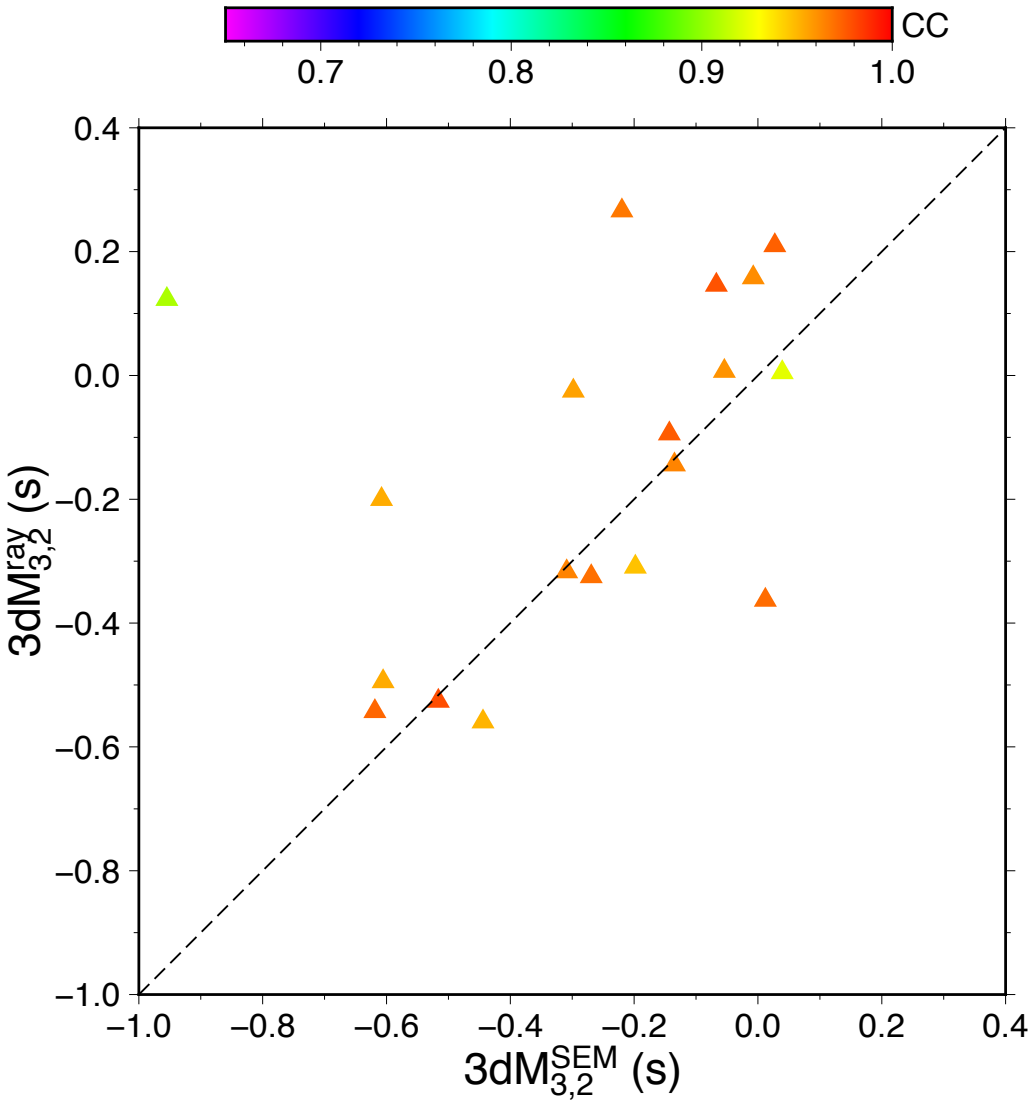

Figure S6. 3D mantle structure corrections to the S3KS-SKKS differential arrival times at 0.05-0.2 Hz. The horizontal axis corresponds to the 3D mantle structure corrections derived from SEM synthetic seismograms and the vertical axis corresponds to the corrections calculated using ray theory. The colors indicate the CC coefficients measured on the SEM synthetic seismograms. Full results are listed in table S3. The 3D mantle model S40RTS (Ritsema et al., 2011) is used for both ray theoretical and SEM estimates.

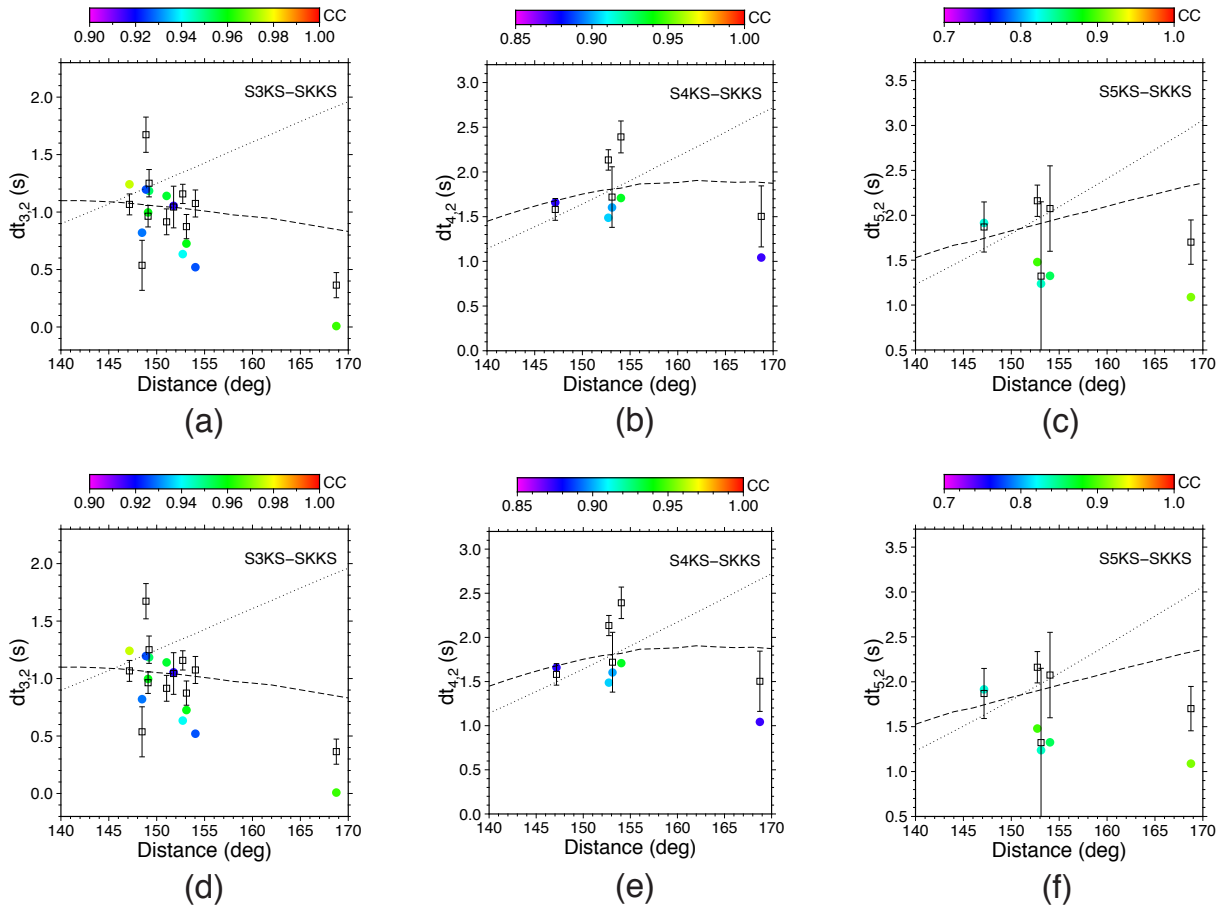

Figure S7. SmKS time delays measured at 0.05-0.7 Hz (a, b and c) and 0.1-0.7 Hz (d, e and f). The empty squares represent the SmKS (m= 3 in a, 4 in b and 5 in c) time delays measured on the data. The time delays are relative to SmKS-SKKS differential arrival times predicted by PREM. Note that error bars are symmetric and in a few cases extend beyond the limits of the figure. The solid circles are SmKS time delays after the 3D mantle structure corrections based on ray theory and S40RTS model. The color shows the corresponding CC values measured on the data. More detailed information are displayed in Tables S3-5. The black dashed line in each figure is the corresponding SmKS time delay predicted by KHMOC (Kaneshima & Helffrich, 2013). The black dotted lines show the EPOC predictions. The source depth used in the KHMOC and EPOC predictions is 150 km. (a) S3KS time delays for data at 0.05-0.7 Hz. (b) S4KS time delays for data at 0.05-0.7 Hz. (c) S5KS time delays for data at 0.05-0.7 Hz. (d) S3KS time delays for data at 0.1-0.7 Hz. (e) S4KS time delays for data at 0.1-0.7 Hz. (f) S5KS time delays for data at 0.1-0.7 Hz.

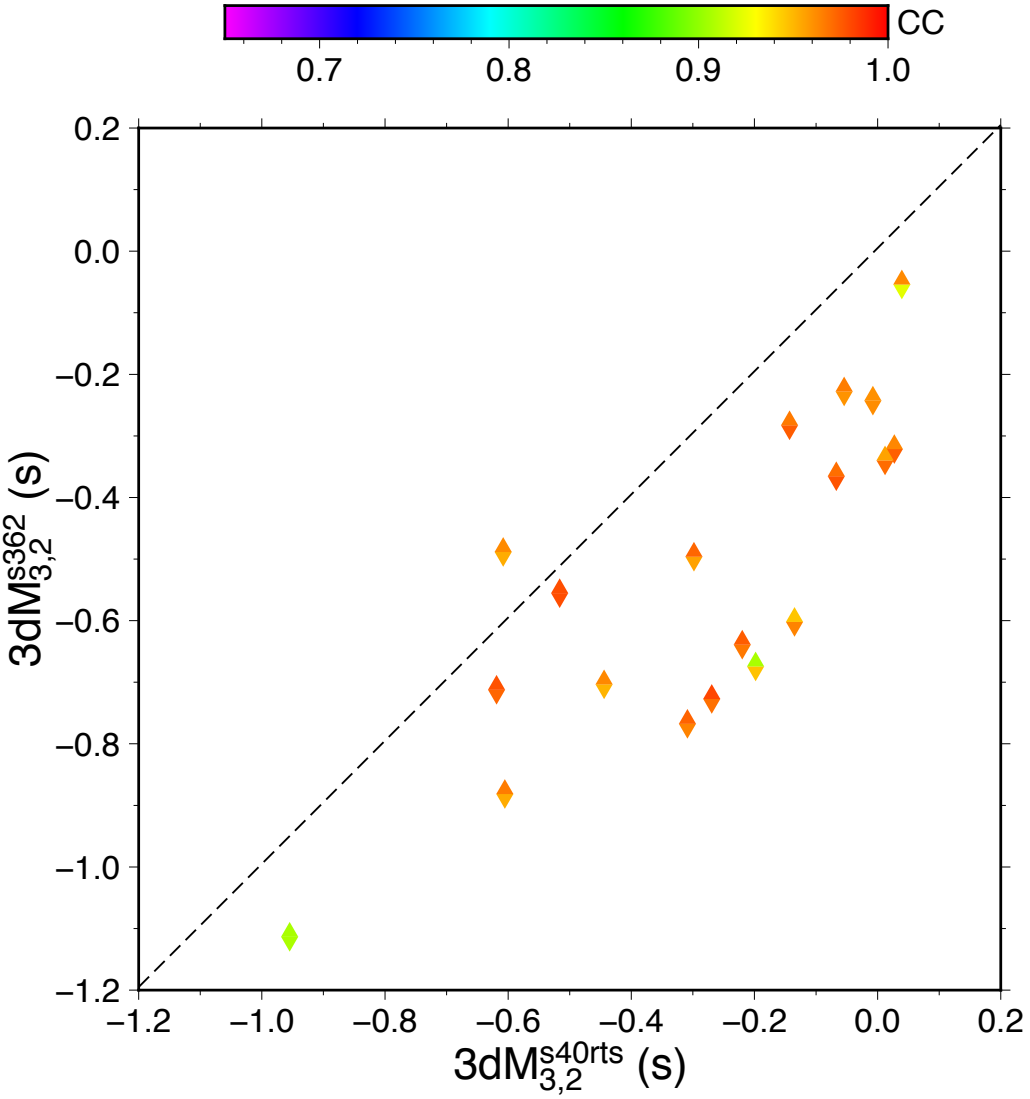

Figure S8. 3D mantle structure corrections using two 3D mantle models of S40RTS (Ritsema et al., 2011) and S362ANI (Kustowski et al., 2008). The x-axis corresponds to the 3D mantle structure corrections to the S3KS-SKKS differential arrival times derived from SEM synthetic seismograms (0.05-0.2 Hz) using S40RTS. The y-axis corresponds to the corrections from SEM synthetic seismogram using S362ANI. The color of the lower half of each diamond shows the CC coefficient corresponding to S40RTS while the color of the upper half is the CC for S362ANI.

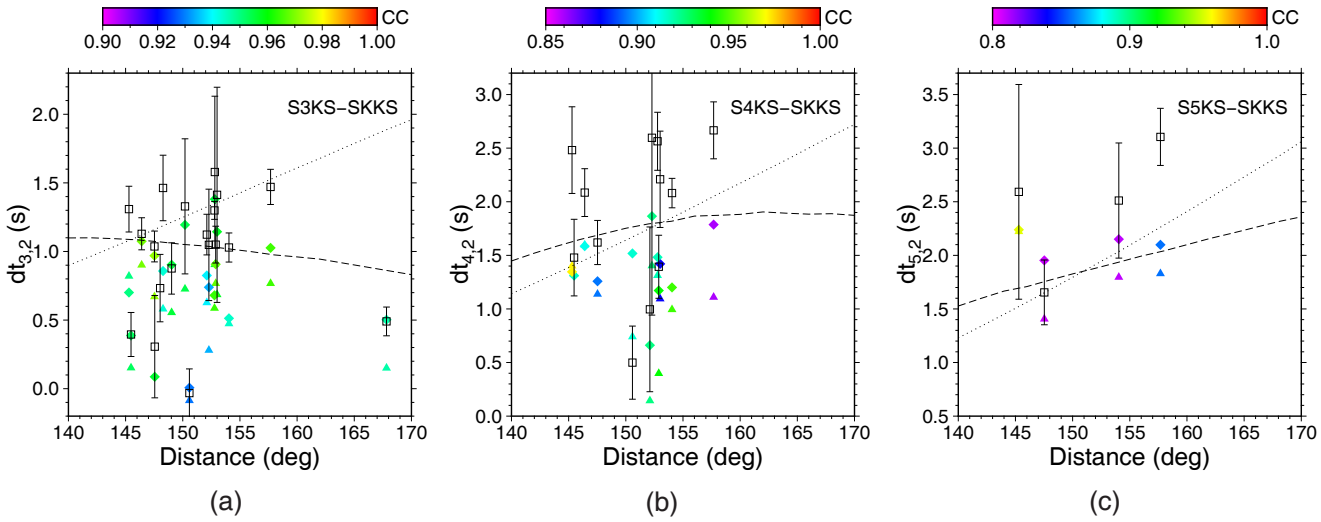

Figure S9. SmKS time delays measured at 0.05-0.2 Hz. The empty squares represent the SmKS (m= 3 in a, 4 in b and 5 in c) time delays measured on the data. The time delays are relative to SmKS-SKKS differential arrival times predicted by PREM. Note that error bars are symmetric and in a few cases extend beyond the limits of the figure. The solid diamonds are SmKS time delays after the 3D mantle structure corrections based on the SEM synthetic seismograms using S40RTS model. The solid triangles are SmKS time delays after the corrections measured on the SEM synthetic seismograms using S362ANI. The color shows the corresponding CC values measured on the data. The black dashed line in each figure is the corresponding SmKS time delay predicted by KHOMC (Kaneshima & Helffrich, 2013). The black dotted lines show the predictions using EPOC (Irving et al., 2018). The source depth used in the KHMOC and EPOC predictions is 150 km. (a) S3KS time delays. (b) S4KS time delays. (c) S5KS time delays.

Table S1. Partial parameters of the GCMT solutions of the earthquakes used in this study. We re-estimate the source durations using global teleseismic P-waves (see Section S5 and Fig. S4).

Event ID	Date	Time	Latitude (°)	Longitude (°)	Depth (km)	Mw	Dur (s)
#010428	2001/04/28	04:50:01.90	-18.07	-176.68	367.4	6.8	9
#010526	2001/05/26	10:57:31.00	-20.25	-177.65	413.9	6.3	7
#060226	2006/02/26	03:08:31.79	-23.59	-179.82	553.9	6.4	3
#071005	2007/10/05	07:17:58.95	-25.27	179.50	540.8	6.5	5
#071016	2007/10/16	21:05:46.75	-25.70	179.72	512.4	6.6	4
#110729	2011/07/29	07:42:28.03	-23.78	179.92	539.0	6.7	5
#120124	2012/01/24	00:52:09.11	-25.00	178.72	581.8	6.3	4
#140721	2014/07/21	14:54:46.87	-19.68	-178.32	627.1	6.9	7
#141101	2014/11/01	18:57:29.87	-19.76	-177.61	445.4	7.1	9
#150123	2015/01/23	03:47:33.40	-17.06	168.36	231.0	6.8	6
#160924	2016/09/24	21:28:48.35	-19.77	-178.15	606.8	6.9	10

Table S2. Results measured on the data (0.05-0.2 Hz) from the fifth iteration. The parameter Ntr gives the number of traces used in this bin. $A_{3,2}$ is the S3KS/SKKS amplitude ratios and $dt_{3,2}$ represents the S3KS time delays relative to S3KS-SKKS differential travel times predicted by PREM. $CC_{3,2}$ is the CC values between SKKS and S3KS. The last six parameters are the measurements for S4KS and S5KS.

Event ID	Bin	Ntr	$A_{3,2}$	$dt_{3,2}(s)$	$CC_{3,2}$	$A_{4,2}$	$dt_{4,2}(s)$	$CC_{4,2}$	$A_{5,2}$	$dt_{5,2}(s)$	$CC_{5,2}$
#010428	bin1	20	0.40	-0.03	0.93	0.26	0.50	0.92	0.12	0.32	0.73
#010428	bin2	17	0.35	1.58	0.96	0.26	2.17	0.83	0.14	5.00	0.28
#010526	bin1	16	0.50	1.12	0.94	0.50	1.00	0.92	0.33	-1.83	0.83
#010526	bin2	5	0.68	1.22	0.92	0.42	4.89	0.78	0.42	3.48	0.67
#020819	bin1	11	0.53	2.43	0.50	0.32	-5.00	0.41	0.36	-5.00	0.49
#060226	bin1	9	0.56	2.42	0.52	0.62	3.75	0.74	0.47	-1.84	0.68
#060226	bin2	6	0.58	1.44	0.94	0.31	2.56	0.82	0.25	2.18	0.61
#071005	bin1	19	0.50	1.05	0.93	0.35	2.60	0.92	0.14	2.41	0.67
#071005	bin2	12	0.56	1.41	0.96	0.38	2.21	0.88	0.30	3.22	0.78
#071005	bin3	26	0.53	1.04	0.97	0.28	1.62	0.89	0.23	1.65	0.81
#071016	bin1	34	0.44	1.03	0.94	0.31	2.08	0.95	0.14	2.51	0.81
#071016	bin2	12	0.48	1.33	0.95	0.24	2.11	0.84	0.21	2.73	0.75
#071016	bin3	23	0.41	0.88	0.96	0.19	1.81	0.85	0.15	2.14	0.69
#110729	bin1	57	0.40	1.30	0.96	0.28	2.56	0.92	0.20	2.72	0.77
#110729	bin2	31	0.71	2.83	0.86	0.37	3.68	0.73	0.24	4.54	0.13
#110729	bin3	26	0.52	1.13	0.97	0.20	2.09	0.91	0.16	2.35	0.80
#110729	bin4	29	0.45	0.49	0.95	0.22	2.04	0.71	0.15	1.74	0.60
#120124	bin1	42	0.41	1.47	0.96	0.18	2.67	0.86	0.21	3.11	0.86
#120124	bin2	10	0.46	0.39	0.95	0.26	1.48	0.92	0.11	2.36	0.56
#140721	bin1	19	0.49	0.73	0.96	0.16	2.49	0.72	0.21	1.70	0.83
#140721	bin2	8	0.67	2.15	0.93	0.78	3.60	0.97	0.46	0.21	0.90
#140721	bin3	5	0.53	1.50	0.91	0.24	2.46	0.67	0.22	5.00	0.70
#141101	bin1	48	0.37	0.11	0.85	0.31	0.18	0.96	0.13	-2.69	0.87
#141101	bin2	37	0.35	1.05	0.97	0.19	1.39	0.94	0.07	2.54	0.69
#141101	bin3	19	0.57	1.46	0.94	0.22	3.11	0.83	0.16	3.92	0.65
#141101	bin4	25	0.48	1.30	0.95	0.34	2.48	0.97	0.17	2.59	0.96
#141101	bin5	12	0.42	0.31	0.96	0.18	-1.18	0.85	0.23	-5.00	0.89
#150123	bin1	42	0.53	1.55	0.89	0.36	2.55	0.90	0.27	1.20	0.86
#160924	bin1	17	0.50	0.57	0.83	0.44	1.46	0.79	0.36	-2.71	0.67
#160924	bin2	10	0.46	0.95	0.77	0.30	1.71	0.87	0.14	-3.47	0.80

Table S3. S3KS time delays with high CC values at 0.05-0.2 Hz. The parameter Ntr is the number of traces used in this bin and $Dist$ represents the median distance of the bin. Note that $dt_{3,2}$ is time delay relative to S3KS-SKKS differential travel time predicted by PREM. $dt_{3,2}$ and $CC_{3,2}$ are the measurements on the data (see Table S2). $3dM^{ray}$ is the 3D mantle corrections to S3KS time delays using ray theory and the S40RTS model (Ritsema et al., 2011). $dt_{3,2}^{ray}$ is equal to $dt_{3,2}$+$3dM^{ray}$ and gives the S3KS time delays after the 3D mantle corrections using ray theory. Similarly, $3dM^{SEM}$ represents the corrections based on SEM synthetic seismograms using th S40RTS model and $dt_{3,2}^{SEM}$ is the corrected S3KS time delays. The S3KS/SKKS amplitude ratios measured on the SEM synthetic seismograms are listed in the $A_{3,2}^{SEM}$ column and $CC_{3,2}^{SEM}$ shows the corresponding CC values.

Event ID	Bin	Ntr	$Dist(^\circ)$	$dt_{3,2}(s)$	$CC_{3,2}$	$dt_{3,2}^{ray}(s)$	$3dM_{3,2}^{ray}$	$dt_{3,2}^{SEM}(s)$	$3dM_{3,2}^{SEM}$	$A_{3,2}^{SEM}$	$CC_{3,2}^{SEM}$
#010428	bin1*	20	150.58	-0.03±0.18	0.93	-0.03	0.00	0.01	0.04	0.35	0.92
#010428	bin2	17	152.81	1.58±0.55	0.96	1.27	-0.31	1.38	-0.20	0.37	0.95
#010526	bin1	16	152.10	1.12±0.15	0.94	1.10	-0.03	0.82	-0.30	0.39	0.96
#071005	bin1	19	152.28	1.05±0.41	0.93	0.73	-0.32	0.74	-0.31	0.51	0.96
#071005	bin2	12	153.00	1.41±0.78	0.96	1.09	-0.32	1.14	-0.27	0.46	0.97
#071005	bin3	26	147.53	1.04±0.11	0.97	1.18	0.15	0.97	-0.07	0.43	0.98
#071016	bin1	34	154.04	1.03±0.11	0.94	0.50	-0.53	0.51	-0.52	0.50	0.98
#071016	bin2	12	150.20	1.33±0.49	0.95	1.18	-0.14	1.19	-0.13	0.45	0.96
#071016	bin3	23	149.02	0.88±0.19	0.96	1.09	0.21	0.90	0.03	0.40	0.97
#110729	bin1	57	152.78	1.30±0.06	0.96	0.76	-0.54	0.68	-0.62	0.48	0.97
#110729	bin3	26	146.41	1.13±0.12	0.97	1.14	0.01	1.07	-0.05	0.42	0.96
#110729	bin4	29	167.82	0.49±0.10	0.95	0.13	-0.36	0.50	0.01	0.45	0.97
#120124	bin1	42	157.68	1.47±0.13	0.96	0.91	-0.56	1.03	-0.44	0.41	0.95
#120124	bin2	10	145.48	0.39±0.16	0.95	0.55	0.16	0.39	-0.01	0.41	0.96
#140721	bin1	19	148.02	0.73±0.25	0.96	0.86	0.12	-0.22	-0.95	0.30	0.91
#141101	bin2	37	152.88	1.05±0.13	0.97	0.96	-0.09	0.91	-0.14	0.39	0.97
#141101	bin3	19	148.28	1.46±0.24	0.94	0.97	-0.49	0.86	-0.61	0.44	0.95
#141101	bin4	25	145.29	1.31±0.17	0.95	1.11	-0.20	0.70	-0.60	0.41	0.95
#141101	bin5	12	147.55	0.31±0.37	0.96	0.57	0.27	0.09	-0.22	0.40	0.97

* This bin has $A_{3,2} < A_{4,2}$ and therefore fails the quality test, which requires an amplitude decay of $A_{3,2} > A_{4,2} > A_{5,2}$.

Table S4. S4KS time delays with high quality at 0.05-0.2Hz.

Event ID	Bin	Ntr	$Dist(^\circ)$	$dt_{4,2}(s)$	$CC_{4,2}$	$dt^{ray}_{4,2}(s)$	$3dM^{ray}_{4,2}$	$dt^{SEM}_{4,2}(s)$	$3dM^{SEM}_{4,2}$	$A^{SEM}_{4,2}$	$CC^{SEM}_{4,2}$
#010428	bin1*	20	150.58	0.50±0.34	0.92	0.55	0.05	1.52	1.02	0.42	0.96
#010526	bin1	16	152.10	1.00±0.77	0.92	1.05	0.06	0.66	-0.33	0.22	0.95
#071005	bin1	19	152.28	2.60±1.65	0.92	2.21	-0.39	1.86	-0.73	0.27	0.92
#071005	bin2	12	153.00	2.21±0.45	0.88	1.79	-0.42	1.42	-0.79	0.28	0.97
#071005	bin3	26	147.53	1.62±0.21	0.89	1.66	0.04	1.26	-0.36	0.30	0.97
#071016	bin1	34	154.04	2.08±0.14	0.95	1.41	-0.67	1.20	-0.88	0.29	0.95
#110729	bin1	57	152.78	2.56±0.27	0.92	1.89	-0.68	1.48	-1.08	0.26	0.94
#110729	bin3	26	146.41	2.09±0.22	0.91	1.97	-0.12	1.59	-0.50	0.31	0.97
#120124	bin1	42	157.68	2.67±0.27	0.86	1.84	-0.83	1.79	-0.88	0.20	0.94
#120124	bin2	10	145.48	1.48±0.36	0.92	1.52	0.05	1.31	-0.17	0.22	0.92
#141101	bin2	37	152.88	1.39±0.29	0.94	1.35	-0.04	1.17	-0.22	0.22	0.93
#141101	bin4	25	145.29	2.48±0.40	0.97	2.10	-0.39	1.35	-1.13	0.29	0.96

* This bin has $A_{3,2} < A_{4,2}$ and therefore fails the quality test, which requires an amplitude decay of $A_{3,2} > A_{4,2} > A_{5,2}$.

Table S5. S5KS time delays with high quality at 0.05-0.2Hz.

Event ID	Bin	Ntr	$Dist(^\circ)$	$dt_{5,2}(s)$	$CC_{5,2}$	$dt^{ray}_{5,2}(s)$	$3dM^{ray}_{5,2}$	$dt^{SEM}_{5,2}(s)$	$3dM^{SEM}_{5,2}$	$A^{SEM}_{5,2}$	$CC^{SEM}_{5,2}$
#010526	bin1	16	152.10	-1.83±1.41	0.83	-1.68	0.16	-1.69	0.14	0.09	0.73
#071005	bin3	26	147.53	1.65±0.30	0.81	1.68	0.03	1.95	0.30	0.15	0.90
#071016	bin1	34	154.04	2.51±0.54	0.81	1.76	-0.75	2.15	-0.36	0.17	0.86
#120124	bin1	42	157.68	3.11±0.27	0.86	2.17	-0.94	2.10	-1.01	0.13	0.83
#141101	bin4	25	145.29	2.59±1.00	0.96	2.13	-0.46	2.24	-0.35	0.17	0.95